

Energy mapping of Jupiter's auroral electrons from Juno/UVS data using a new H₂ UV emission model

B. Benmahi¹, B. Bonfond¹, B. Benne², D. Grodent¹, V. Hue³, G. R. Gladstone⁴, G. Gronoff^{5,6}, J. Liliensten⁷, G. Sicorello¹, L. A. Head¹, M. Barthélemy⁷, C. Simon Wedlund⁸, R. S. Giles⁴, and T. K. Greathouse⁴

¹ Laboratory for Planetary and Atmospheric Physics, STAR Institute, University of Liege, Liege, Belgium
e-mail: bilal.benmahi@uliege.be

² The University of Edinburgh, School of Geosciences, Edinburgh, United Kingdom.

³ Aix-Marseille Université, CNRS, CNES, Institut Origines, LAM, Marseille, France.

⁴ Space Science and Engineering Division, Southwest Research Institute, San Antonio, Texas, USA.

⁵ NASA Langley Research Center, Hampton, Va, USA.

⁶ Science Systems And Applications Inc., Hampton, Va, USA

⁷ Univ. Grenoble Alpes, CNRS, IPAG, 38000 Grenoble, France.

⁸ Institut für Weltraumforschung (IWF), Austrian Academy of Sciences, Graz, Austria.

Received 16 November 2023 ; Accepted 07 February 2024

ABSTRACT

Context. Juno, which studies the Jovian system, continues to expand our knowledge of Jupiter's magnetosphere and its environment. Thanks to onboard instruments such as Jupiter Energetic Particle Detector Instrument (JEDI) and Jovian Auroral Distributions Experiment (JADE), in situ measurements have allowed us to derive a realistic representation of charged particle energy distributions precipitating in the auroral regions. Because of the distance between Juno's measurement location and the position of impact of the charged particles, where auroral emissions are produced, these energetic distributions of magnetospheric particles are likely to be affected by various phenomena such as wave-particle interactions on their way from Juno to the atmosphere. These processes can accelerate or decelerate the particles, changing their average energies. Hence, the energy distributions of particles measured at Juno's altitude are likely different from those at auroral altitudes.

Aims. In this study we develop a UV emission model, combined with an electron transport model, that allows us to relate the auroral emission spectra of H₂ molecules with the energy distribution of impinging electrons.

Methods. Thanks to observations of the Jovian aurora by the Ultraviolet Spectrograph (UVS) on board Juno, we determined the characteristic energies of electrons precipitating in auroral regions during perijove 32. We modeled the relationship between color ratio (CR) and the characteristic energy of precipitating electrons. Initially, we considered mono-energetic electron fluxes. In a second step, we considered fluxes governed by a kappa distribution.

Results. We derived characteristic energy maps for electrons precipitating in Jupiter's auroral regions. In comparison with similar previous studies based on Space Telescope Imaging Spectrograph on board Hubble Space Telescope (HST/STIS) observations, we find that modeling the CR with a mono-energetic distribution leads to a systematic underestimation of the average energy of electrons precipitating in the auroral regions by a factor of 3-5.

Conclusions. In this study we show that it is possible to derive a more realistic estimate of electron energy flux distributions at auroral altitudes.

Key words. Jupiter, UV Spectroscopy, Aurora, Magnetosphere, Electron transport.

1. Introduction

Observations of Jupiter in the UV range have revealed the existence of extremely bright polar auroral phenomena. The first observational evidence of these phenomena was provided by observations of UV emissions from atomic hydrogen (H Lyman- α emission) and molecular hydrogen (Lyman band emissions: $B^1\Sigma_u^+ \rightarrow X^1\Sigma_g^+$ and Werner bands: $C^1\Pi_u \rightarrow X^1\Sigma_g^+$) during the flyby of the Voyager 1 spacecraft (Broadfoot et al. 1979). In addition, Jovian aurorae have been extensively studied by the International Ultraviolet Explorer (IUE) for approximately two decades (Clarke et al. 1980; Livengood et al. 1992; Gladstone & Skinner 1989; Harris et al. 1996). These observations, in the mid-UV range (between 120 nm and 170 nm), have allowed the characterization of the power of the aurorae, and also the study of their structure, variability, and intensity. Thanks to these spectral

measurements, the first models of UV auroral emissions were developed (Yung et al. 1982; Gladstone & Skinner 1989). This demonstrated that the direct excitation of molecular hydrogen by electrons and absorption of CH₄ below 140 nm could, overall, reproduce UV auroral spectra well in the range of 120 nm to 170 nm.

The Hubble Space Telescope (HST) has dramatically contributed to the study of Jovian aurorae, thanks to observations of auroral structures by the Faint Object Camera (FOC) (Dols et al. 1992; Gérard et al. 1993, 1994; Prangé et al. 1998) and Wide Field Planetary Camera 2 (WFPC2) (Clarke et al. 1996, 1998; Grodent et al. 1997), as well as UV spectral observations by the Space Telescope Imaging Spectrograph (STIS) on board HST (HST/STIS) (Gustin et al. 2002). Despite these numerous studies, the morphology of the Jovian aurora remains very difficult to describe in an exhaustive way as their structure is complex

and includes spatially and temporally variable substructures (see Grodent 2015). However, these various observations have made it possible to characterize, in a simple way, the morphology of Jupiter's aurorae: the main auroral emissions form a partially closed oval, with highly variable structures in the polar region inside the main emissions and equatorward emission structures outside, including the footprints of Io, Europa, and Ganymede.

The auroral emission on Jupiter occurs due to the interaction between its magnetosphere and atmosphere. This interaction leads to the precipitation of energetically charged particles along magnetic field lines. In these regions, electrons are the primary species that precipitate, as stated by Rego et al. (2001). In the UV domain [80 nm, 180 nm], Jupiter's auroral spectral emission is dominated by H Lyman- α emission and the de-excitation of H₂ molecules by electronic transitions: $B^1\Sigma_u^+ \rightarrow X^1\Sigma_g^+$ (Lyman bands) and the R¹, P, and Q branches of the $C^1\Pi_u \rightarrow X^1\Sigma_g^+$ transition (Werner bands). Moreover, this spectral emission is strongly influenced by the presence of hydrocarbons in Jupiter's atmosphere, including methane, which mainly absorbs UV photons below 140 nm.

The main studies resulting from the various spectral observations of Jupiter's auroral regions are those concerning the energy characterization of the electrons precipitating in these regions. Although numerous probes have studied Jupiter's magnetosphere at the spacecraft altitude, such as Voyager (Russell 1993), Ulysses (Zarka 1998), Galileo, Cassini-Huygens (Hansen et al. 2004), and the New Horizon flyby (Krupp 2007), measurements and observations of magnetospheric plasma have never characterized the energy distributions of the electrons that precipitate immediately above the polar aurora's altitudes. There are complex processes, such as acceleration by inertial Alfvén waves (Hess et al. 2010, 2013; Saur et al. 2018) and by whistler waves (Elliott et al. 2018), and ion and electron inverted-V structures (Mauk et al. 2017; Clark et al. 2017; Mauk et al. 2018), that alter the energy flux distribution of electrons between the altitude of measurement and the high-latitude ionospheric regions. Thus, to measure the shape of the energy flux distributions of electrons precipitating in auroral regions, only low altitude measurements can be effective.

For the present study we used a combination of spectral observations and modeling to study these characteristics. The method we adopted is phenomenological; it was first proposed by Yung et al. (1982) and is based on the far-UV (FUV) color ratio (CR) of the auroral H₂ emission spectrum. Our aim is to take advantage of the wavelength-dependent absorption of auroral emission by hydrocarbons such as CH₄, which is the third most abundant molecule in Jupiter's stratosphere (e.g., Moses et al. 2005; Hue et al. 2018). Thus, by considering the unabsorbed part of the H₂ emission spectrum, we can derive a CR that allows us to characterize the energy distributions of the electron fluxes that precipitate in these regions, as well as their characteristic energies. In the case of absorption by methane, this ratio is defined by $CR = \frac{I(155\text{nm}-162\text{nm})}{I(123\text{nm}-130\text{nm})}$ (Gustin et al. 2013), where $I(\lambda_{min} - \lambda_{max}) = \int_{\lambda_{min}}^{\lambda_{max}} I d\lambda$ and I is the spectrum flux intensity and where the ranges [123 nm–130 nm] and [155 nm–162 nm] represent, respectively, a range absorbed by CH₄ and the unabsorbed part of the spectrum. This allows us to infer, for a fixed emission angle, that over the range [123 nm–130 nm] increasing spectral absorption means that electrons penetrate deeper into

the atmosphere before being thermalized, and are therefore more energetic. This method is very advantageous since it does not require the use of absolute spectra of auroral emission as CR can be measured using only arbitrary units within the same spectra.

The relationship between the CR and the characteristic electron energy E_0 ($CR(E_0)$) is monotonic, and is modeled using a combination of an electronic transport model and a H₂ UV emission model in the auroral regions. This supposes modeling the excitation of H₂ molecules by electron collisions, before calculating their de-excitation from rovibrational levels producing UV emissions. Each modeled spectrum allows the CR to be linked to the characteristic energy of the electrons precipitated in the atmospheric model. Finally, by varying the characteristic energy of the electrons in the transport model, we build the relationship $CR(E_0)$, which is compared with the observed CR to estimate E_0 .

Several studies (e.g., Trafton et al. 1994, 1998; Grodent et al. 2001; Gustin et al. 2002; Ajello et al. 2005; Gérard et al. 2014; Gustin et al. 2016) have used this technique to characterize the electron energy in auroral regions using HST observations. In most of these studies, the auroral electron transport was modeled by initial mono-energetic, Maxwellian, or kappa phenomenological flux distributions (see the example by Gustin et al. 2016). However, despite the high spectral resolution of the HST/STIS observations exploited in previous studies, the signal-to-noise ratio (S/N) was limited and the spatial coverage of the aurora was partial and highly dependent on the planet's tilt axis. Thus, it is only since Juno's arrival (Bolton et al. 2017) and the Ultraviolet Spectrograph (UVS) observations (Gladstone et al. 2017; Bonfond et al. 2017) that we have had full access to Jupiter's northern and southern local time. In addition, UVS observations are highly spatially resolved near Jupiter's closest approach, with a spectral resolution of around 0.6 nm–2.4 nm. This allows correct spectral sampling with a better S/N than the HST/STIS observations.

In this study we map for the first time the characteristic energy of electrons precipitating in Jupiter's auroral regions using Juno/UVS observations. We have developed a new UV emission model of H₂, inspired by the models of Dols et al. (2000), Gustin et al. (2002) and Menager (2011), in a more optimized version that takes into account nine H₂ electronic states including cascade excitation and auto-absorption in the Lyman and Werner bands. This model is now available for the community, and can be used in every electron transport model. The excited states of H₂ are calculated through the outputs of our TransPlanet electronic transport model (Stamnes & Rees 1983b; Gronoff 2009; Menager 2011) and Benmahi (2022). Additionally, for the CR modeling, we modeled the electronic transport using mono-energetic initial electron flux distributions and a kappa distribution (Coumans et al. 2002; Scherer et al. 2018) derived from Jupiter Energetic Particle Detector Instrument (JEDI) measurements obtained during the first 20 perijoves (PJs) (Salveter et al. 2022) of the Juno mission.

The outline of our study is as follows. We first describe the electronic transport model and the UV emission model. In the second step, we describe the Juno/UVS observations and explain the mapping of the characteristic energy method. Finally, we present our results and discussions before concluding.

¹ The R branch results from a variation in the rotational quantum number $\Delta J = J_{ini} - J_{fin} = +1$. The P branch corresponds to the variation $\Delta J = -1$. The Q branch corresponds to the variation $\Delta J = 0$.

149 **2. Models**150 **2.1. Electron transport model: TransPlanet**

151 To simulate electron precipitation in Jupiter’s atmosphere, we
 152 used the TransPlanet model developed in collaboration with the
 153 Institut de Planétologie et d’Astrophysique de Grenoble (IPAG).
 154 This transport code was first created by Lilensten et al. (1989)
 155 and was modified and improved by Blelly et al. (1996) for appli-
 156 cation to terrestrial cases (Simon et al. 2007). The model was di-
 157 versified and adapted to several planets over the years. The core
 158 of this algorithm was used in Trans-Mars (Witasse et al. 2002,
 159 2003; Simon et al. 2009; Nicholson et al. 2009), Trans-Venus
 160 (Gronoff et al. 2007, 2008), Trans-Titan (Lilensten et al. 2005a,b;
 161 Gronoff et al. 2009a,b), Trans-Uranus, Trans-Jupiter (Menager
 162 et al. 2010), Aeroplanets Gronoff et al. (2012a,b, 2014), and re-
 163 cently Trans-Planet (Benmahi 2022). The Trans* code core is di-
 164 vided into two parts: a kinetic part that calculates the interaction
 165 of precipitating electrons with atmospheric particles and a fluid
 166 part that is implemented only in the TRANSCAR and TRANS4
 167 versions (Lathuillere et al. 1997; Simon et al. 2007), which uses
 168 a 13-moment fluid closure description, calculating, among other
 169 parameters, the number density, velocity, heat flux, and plasma
 170 temperature (of electrons and ions). Thus, in the Trans* version
 171 we used for this study, there is no fluid part. Compared with the
 172 various existing electron transport codes, Trans* allows multi-
 173 stream modeling of electron transport with electron scattering
 174 over a wide range of electron energies and pitch angles. The
 175 electronic transport model we use in this study is detailed in
 176 Appendix A. The uncertainties in that class of models has been
 177 studied in Gronoff et al. (2012a,b) and highlighted that the cross
 178 sections are one of the major sources of uncertainties. Efforts
 179 have been made to improve cross section datasets through the
 180 Atomic and Molecular Cross section for Ionization and Aurora
 181 Database (ATMOCIAD) Gronoff et al. (2021) and also through
 182 comparison with the experimental data Wedlund et al. (2011).

183 For this study we modeled electron transport taking into
 184 account only magnetospheric electron precipitation. Secondary
 185 electrons resulting from ionization by solar UV radiation are ne-
 186 glected as their penetration capacity in Jupiter’s atmosphere is
 187 low and considerably above the homopause of the hydrocarbons
 188 considered, such as CH₄, C₂H₂, or C₂H₆.

189 The atmospheric model of the auroral region we used to
 190 model electronic transport is described in Grodent et al. (2001)
 191 and presented in Fig. 1. This model is 1D, and takes into account
 192 the majority of neutral species (H, H₂, He, and CH₄) that pre-
 193 dominate in Jupiter’s atmosphere. It extends from the tropopause
 194 at a pressure of ~100 mbar (altitude ~100 km above the cloud
 195 level) to the upper thermosphere (altitude ~2,300 km above the
 196 cloud level), corresponding to a pressure of ~10⁻⁹ mbar. The
 197 initial density of thermalized electrons considered in the model
 198 is that obtained by Hinson et al. (1998) from radio occultations
 199 during the Voyager 2 flyby. Because of the limited data available,
 200 the initial electron temperature is thought to be similar to the
 201 temperature of the neutral atmosphere. In addition, as the atmo-
 202 spheric model used is 1D, we do not take into account any spatial
 203 or temporal variability in the abundance of neutral species in au-
 204 ral regions, particularly the variability of CH₄. Hence, since
 205 methane is the only tracer used in this study to model CR, any
 206 variability in its abundance can influence the CR. Thus, in this
 207 study we consider a homogeneous and steady chemical compo-
 208 sition in Jupiter’s whole aurora, which probably represents a sig-
 209 nificant approximation.

210 The electron-matter interactions considered in the physics of
 211 electron transport are the elastic interactions in which total ki-

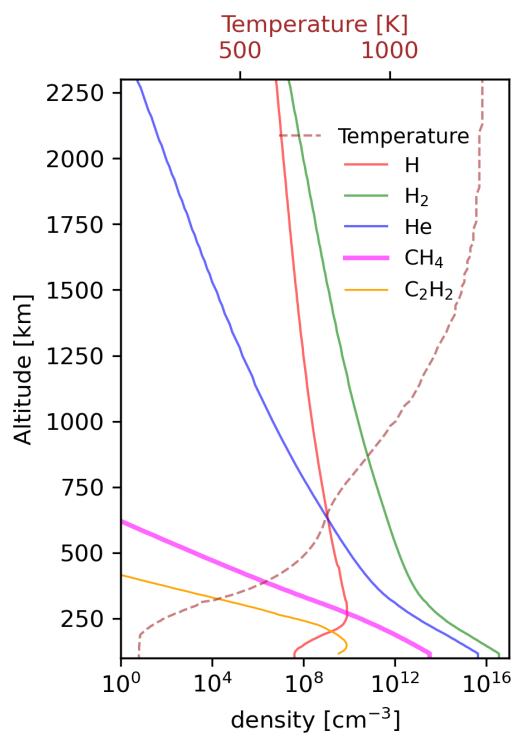


Fig. 1. Atmospheric model described by Grodent et al. (2001), which considers only the neutral compounds (H, H₂, He, CH₄, and C₂H₂) that predominate in Jupiter’s atmosphere. For electronic transport modeling, only H, H₂, He, and CH₄ compounds were considered. For the UV emission model, spectral absorption by CH₄ and C₂H₂ was taken into account.

212 netic energy is conserved, and the inelastic interactions of elec-
 213 trons with atmospheric particles illustrated in Table 1. The elas-
 214 tic cross sections $e+H$ (Kingston & Walters 1980), $e+He$ (Porter
 215 et al. 1987), $e+H_2$ (Muse et al. 2008), and $e+CH_4$ (Davies et al.
 216 1989) considered are measured in different energy ranges, which
 217 may not entirely cover the energy grid² ranges needed for the
 218 electron transport modeling. For cross sections that do not cover
 219 the entire energy grid considered, we used power-law extrapo-
 220 lations to fill the gap. Above 400 eV the cross section $\sigma(E)$ is
 221 considered to be proportional to $E^{-0.65}$ (Wedde & Strand 1974),
 222 and above 2.2 keV the cross section is proportional to E^{-1} (Rees
 223 1989). For inelastic cross sections we used the same approach
 224 as for elastic collisions. The power-law evolution of these cross
 225 sections at high energies makes it possible to use a decreasing
 226 logarithmic extrapolation to cover the entire range of the model-
 227 ing energy grid.

228 As described in Appendix A, by solving the Boltzmann
 229 equation we calculate the electron flux $F(z, E)$ as a function of
 230 altitude and electron energy. This flux results from the interac-
 231 tion between magnetospheric electrons precipitating in auroral
 232 regions and the neutral atmospheric particles considered in our
 233 model. To model auroral emission by H₂, we used $F(z, E)$ as an
 234 initial condition in our UV emission model.

² For kappa distributions, we simulate electron transport in the energy range [1 eV, 1 MeV]. For mono-energetic distributions, the electron transport modeling energy ranges are defined by [1 eV, E_0], where E_0 is the characteristic or average energy of the mono-energetic distribution considered.

Table 1. Inelastic electron collision reactions.

| Reactions | Products |
|-------------------------------------|--|
| $e^- + \text{H} \longrightarrow$ | $\text{H}^* + e^-$ $\text{H}^+ + 2e^-$ |
| $e^- + \text{H}_2 \longrightarrow$ | $\text{H}_2^* + e^-$ $\text{H}_2^+ + 2e^-$ $\text{H} + \text{H} + e^-$ $\text{H}^+ + \text{H} + 2e^-$ |
| $e^- + \text{He} \longrightarrow$ | $\text{He}^* + e^-$ $\text{He}^+ + 2e^-$ $\text{He}^{2+} + 3e^-$ |
| $e^- + \text{CH}_4 \longrightarrow$ | $\text{CH}_4^* + e^-$ $\text{CH}_4^+ + 2e^-$ $\text{CH}_3^+ + \text{H} + 2e^-$ $\text{CH}_2^+ + 2\text{H} + 2e^-$ |

2.2. H_2 UV emission model

The R and P branches of the Lyman band of H_2 ($B^1\Sigma_u^+ \longrightarrow X^1\Sigma_g^+$) correspond to the group of rovibrational transitions that produce spectral lines with wavelengths in the range [80 nm–190 nm]. For the Werner band, in addition to the R and P branches, there is a third branch, the Q branch, corresponding to the rovibrational transitions that produce spectral lines in the spectral range [80 nm–160 nm]. There are also other transitions in the UV spectrum of H_2 , at shorter wavelengths, arising from the excited levels $B'^1\Sigma_u^+$, $B''^1\Sigma_u^+$, $D^1\Pi_u^-$, $D^1\Pi_u^+$, $D'^1\Pi_u^-$, and $D'^1\Pi_u^+$, and whose spectral emissions are less intense compared to Lyman and Werner band emissions and lie respectively in the wavelength ranges [85 nm–125 nm], [79 nm–110 nm], [75 nm–110 nm], [75 nm–110 nm], [78 nm–107 nm], and [78 nm–107 nm]. For this study, the H_2 UV emission model in auroral regions we developed takes into account the excited states B , C , B' , B'' , D , and D' , as illustrated here.

According to the atmospheric model used (molecular abundances and thermal profile), we begin by calculating the number density $n(z, X, v_i, J_i)$ at altitude z of the H_2 ground state levels. Thus, assuming that neutral species are thermalized in the atmosphere, the population of the ground state of H_2 follows the Boltzmann distribution given by

$$n(z, X, v_i, J_i) = n_{\text{H}_2}(z) \frac{g_I(i)(2J_i + 1)e^{-\frac{E_i}{k_B T(z)}}}{\sum_k g_I(k)(2J_k + 1)e^{-\frac{E_k}{k_B T(z)}}}, \quad (1)$$

where $n_{\text{H}_2}(z)$ [cm^{-3}] is the density of H_2 at altitude z ; X , v_i , and J_i are respectively the ground electronic level n_i , and the vibrational and rotational quantum numbers; $g_I(i)$ and E_i are respectively the degree of degeneracy of the i state and its energy; k_B is the Boltzmann constant; and $T(z)$ the temperature at altitude z . In the denominator, the sum is made over all the rovibrational ground state levels of H_2 .

An H_2 molecule can be excited into a n_j , v_j , and J_j state by various processes. It can be excited directly by absorbing a photon or by collision with an electron or other atmospheric particles. It can also be excited in this state by cascade de-excitation from higher states. Unlike models of H_2 UV auroral emission that use the Born³ approximation to calculate the excitation rates of the different excited states of H_2 (e.g., Waite et al. 1983),

³ The Born approximation is applied to collisions in which the energy of the incident particle is much greater than the energy of the transition.

in our model we calculate the excitation rates of the considered electronic levels through electronic transport by modeling $e^- + \text{H}_2 \longrightarrow \text{H}_2^* + e^-$ collisions. Transitions from the EF , GK , and HH states to the $X^1\Sigma_g^+$ ground state are forbidden due to the selection rule on $g \longrightarrow g$ transitions, and thus a non-negligible part of the B and C states are populated by these transitions (Liu et al. 2002). In this model we also take into account the excitation of H_2 to the EF , GK , and HH states, as well as the cascade populating of the B and C states. Excitation by other collisional processes with neutral particles is neglected because the atmospheric temperature is not high enough to produce UV emission from collisions of H_2 molecules with neutral particles (e.g., $\text{H}_2 + \text{H}_2 = \text{H}_2^* + \text{H}_2$).

Thus, the volume excitation rate [$\text{cm}^{-3}\text{s}^{-1}$] of a rovibrational state j is a linear combination of the direct excitation rate g_{direct} and the cascade excitation rate g_{cascad} and is given by

$$g(z, n_j, v_j, J_j) = g_{\text{direct}}(z, n_j, v_j, J_j) + g_{\text{cascad}}(z, n_j, v_j, J_j). \quad (2)$$

2.2.1. Direct excitation rate

The direct excitation rate of H_2 by electron collisions is described by the following formula:

$$g_{\text{direct}}(z, n_j, v_j, J_j) = \sum_i n(z, X, v_i, J_i) \int \sigma_{ij}(E) F(z, E) dE. \quad (3)$$

Here the indices j and i are used to identify the upper quantum state and the ground state, respectively; $F(z, E)$ [$\text{cm}^{-2}\text{s}^{-1}\text{eV}^{-1}$] is the electron flux at altitude z with energy between E and $E + dE$ and is modeled by electron transport; $\sigma_{ij}(E)$ [cm^2] is the excitation cross section of the j level from the i level by collision with an electron of energy E (see Liu et al. 1998), and is given by

$$\sigma_{ij}(E) = 4\pi a_0^2 f_{ij} \frac{R_y^2}{E E_{ij}} \left[C_0 \left(\frac{1}{x^2} - \frac{1}{x^3} \right) + \sum_{k=1}^4 C_k (x-1) e^{-k\alpha x} + C_5 + \frac{C_6}{x} + \ln(x) \right], \quad (4)$$

where a_0 is the Bohr radius, $f_{ij} = 1.4992^{-16} A_{ji} E_{ij}^2 \frac{2J_i+1}{2J_j+1}$ (dimensionless) is the oscillator strength of the transition between the i and j levels, and where A_{ji} [s^{-1}] is the Einstein factor of the $j \rightarrow i$ transition; $R_y = \frac{m_e e^2}{8h^2 \epsilon_0^2}$ is the Rydberg constant; E_{ij} is the energy of the transition from the i state to the j state; E is the energy of the incident electron; and $x = \frac{E}{E_{ij}}$. The coefficients C_k and α were obtained experimentally by Liu et al. (1998, 2003) by fitting the excitation functions of the transitions $X^1\Sigma_g^+ \rightarrow B^1\Sigma_u^+$ and $X^1\Sigma_g^+ \rightarrow C^1\Pi_u$ (see Table 2). This parameter was measured for the *ungerade* (odd) and *gerade* (even) levels of the excited states B and C (Liu et al. 1998, 2003). However, these factors were not measured for the B' , B'' , D , D' excited levels, and in this study, following Menager (2011), we consider that these coefficients are also valid for all *ungerade* states.

2.2.2. Cascade excitation rate

Electron collisions populate the g states including the EF , GK , and HH states from the $X^1\Sigma_g^+$ ground state. However, since

Table 2. Electronic excitation function parameters C_k and α .

| | Excitation u levels | Excitation g levels |
|----------|-----------------------|-----------------------|
| C_0 | -0.01555195 | - |
| C_1 | -0.13491574 | 0.50490267 |
| C_2 | -0.02691103 | -0.22500813 |
| C_3 | 0.32786896 | 0.24515133 |
| C_4 | -0.49744809 | 0.10720355 |
| C_5 | -0.435 | -1.7236746 |
| C_6 | 0.435 | - |
| α | 0.17762538 | 0.20983777 |

314 $g \rightarrow g$ are forbidden dipolar transitions, the process of populat-
 315 ing the g levels differs from that of the u levels. This populating
 316 is described by the same relationship (see formula 3) as that for
 317 the u states, but with a different cross section given by

$$\sigma_{ik}(E) = F(x)FC(v_i, J_i, n_k, v_k, J_k)S_r(J_i, J_k), \quad (5)$$

318 where i always refers to the ground state and k to the upper g
 319 state (EF, GK or HH), $x = \frac{E}{E_{ik}}$, E is the energy of the incident
 320 electron, and E_{ik} is the excitation threshold of the $i \rightarrow k$ transi-
 321 tion.

322 The function $F(x)$ describes the excitation of the EF state
 323 from the ground state. **This function is given by the formula**

$$F(x) = \pi a_0^2 \frac{R_y}{E} C_5 \left[\frac{C_0}{C_5} \left(\frac{1}{x^2} - \frac{1}{x^3} \right) + \sum_{m=1}^4 \frac{C_m}{C_5} (x-1) e^{-max} \right. \\ \left. + \left(x - \frac{1}{x} \right) \right], \quad (6)$$

324 where C_m and α are described in Table 2 for transitions to g
 325 states.

326 $F(x)$ was measured only for the excited EF state. For the
 327 GK and HH states, Liu et al. (2002) suggested using the same
 328 excitation function, but multiplying it by a scaling factor to take
 329 into account the excitation efficiency of the different g states.
 330 This factor is 0.8 for GK and 0.35 for HH .

331 $FC(v_i, J_i, n_k, v_k, J_k)$ are the Franck-Condon factors that de-
 332 scribe the overlap of the wave functions of the i and k states and
 333 depend on the quantum numbers v_i and J_i for the ground state
 334 and on n_k, v_k , and J_k for the upper g state. The Franck-Condon
 335 factors follow the selection rules $\Delta J = 0, \pm 2$ and were calculated
 336 by Hervé Abgrall and Evelyne Roueff for Liu et al. (2002).

337 Finally, the function $S_r(J_i, J_k)$ represents the rotational terms
 338 that were calculated by Abgrall et al. (1999) and adopted by Liu
 339 et al. (2003), and are given by the following formula:

$$S_r(J_i, J_k) = \beta \delta_{J_i, J_k} + (1 - \beta) \left[\frac{3(J_k + 1)(J_k + 2)}{2(2J_k + 3)(2J_k + 5)} \delta_{J_i, J_{k+2}} + \right. \\ \left. \frac{J_k(J_k + 1)}{(2J_k - 1)(2J_k + 3)} \delta_{J_i, J_k} + \frac{3J_k(J_k - 1)}{2(2J_k - 1)(2J_k - 3)} \delta_{J_i, J_{k-2}} \right]. \quad (7)$$

340 Here δ is the Kronecker parameter and β is an anisotropy param-
 341 eter for which Liu et al. (2003) recommended a value of 0.6.

342 Cascade excitation of the B and C states mainly increases
 343 emission from the low vibrational levels of B and accentuates
 344 emission from the C state by a smaller proportion. The cascade
 345 excitations of the B', B'', D , and D' states are not taken into ac-
 346 count due to the lack of appropriate data.

2.2.3. Volume emission rate

347

The discrete volume emission rate η [$\text{cm}^{-3}\text{s}^{-1}$] of a transition
 348 from a state j to a state i at altitude z is given by
 349

$$\eta(z, n_j, v_j, J_j \rightarrow X, v_i, J_i) = g(z, n_j, v_j, J_j) \frac{A_{j \rightarrow i}}{A_j^{tot}}, \quad (8)$$

where A_j^{tot} [s^{-1}] is the total Einstein factor of the upper level (j)
 350 and is given by
 351

$$A_j^{tot} = A_j^{cont} + \sum_j A_{j \rightarrow i}, \quad (9)$$

with A_j^{cont} the probability that level j transmits into the contin-
 352 uum. This results in the dissociation of H_2 into two fragments
 353 with kinetic energy E_c , whose expression is given by
 354

$$A_j^{cont} = \sum_{J_i=J_j-1}^{J_j+1} \int_0^\infty A_{j \rightarrow X, E_c, J_i}^{E_c}(E_c) dE_c, \quad (10)$$

where $A_{j \rightarrow X, E_c, J_i}^{E_c}$ [$\text{s}^{-1}\text{eV}^{-1}$] is the differential probability of
 355 dissociation of the j state into two fragments of kinetic energy
 356 E_c and quantum number J_i .
 357

The Einstein factors for the $B \rightarrow X$, $C \rightarrow X$, $B' \rightarrow X$,
 358 and $D \rightarrow X$ transitions were calculated by Abgrall et al. (1994)
 359 and are available in the MOLAT⁴ database. Those for transitions
 360 $B'' \rightarrow X$ and $D' \rightarrow X$ were obtained by personal communication
 361 from H. Abgrall and E. Roueff (Menager et al. 2010). The differ-
 362 ential probability of dissociation $A_{j \rightarrow X, E_c, J_i}^{E_c}(E_c)$ are also available
 363 in the MOLAT database and were calculated by Abgrall et al.
 364 (1997) only for transitions from the B, C, B' , and D states.
 365

The differential volume emission rate in the continuum η_λ^{cont}
 366 [$\text{cm}^{-3}\text{s}^{-1}\text{nm}^{-1}$] comes from excited states above the dissociation
 367 threshold of H_2 . Its intensity at wavelength λ and altitude z after
 368 the dissociation of molecules from excited state j to dissociated
 369 state i is given by
 370

$$\eta_\lambda^{cont}(z, n_j, v_j, J_j \rightarrow v_i, J_i) d\lambda = \\ g(z, n_j, v_j, J_j) \frac{A_\lambda(n_j, v_j, J_j \rightarrow v_i, J_i)}{A_j^{tot}} d\lambda, \quad (11)$$

where $A_\lambda(n_j, v_j, J_j \rightarrow v_i, J_i)$ is the differential probability of di-
 371 sociation of state j , as a function of wavelength λ , and is obtained
 372 directly from $A_{j \rightarrow X, E_c, J_i}^{E_c}(E_c)$.
 373

Quantum transitions $n_j, v_j, J_j \rightarrow n_i, v_i, J_i$ can be represented
 374 by the wavelength λ which corresponds to the energy of each
 375 transition. Thus, by substitution, for discrete transitions we can
 376 write $\eta(z, n_j, v_j, J_j \rightarrow X, v_i, J_i) = \eta^{discr}(z, \lambda)$, and for continuum
 377 transitions we can write $\eta_\lambda^{cont}(z, n_j, v_j, J_j \rightarrow v_i, J_i) = \eta_\lambda^{cont}(z, \lambda)$.
 378

2.2.4. Auto-absorption

379

When an emitted photon from an excited state of H_2 is energetic
 380 enough to excite an H_2 molecule initially in the ground state, it
 381 can be reabsorbed by H_2 to emit another photon of lower energy.
 382

⁴ <https://molat.obspm.fr/indexFR.php?page=pages/menuSpectreMol.php>

383 This self-absorption therefore tends to attenuate the UV emis- 424
384 sion spectrum toward short wavelengths (below 120 nm) and 425
385 amplify it toward low-energy wavelengths. To take account of 426
386 this phenomenon in the model we describe here, we used the re- 427
387 sults of Jonin et al. (2000), who experimentally studied the UV 428
388 spectrum of H₂ in the wavelength range [90 nm; 120 nm]. Thus, 429
389 considering the volume emission rate $\eta_{j \rightarrow i}(z_0)$ at altitude z_0 by 430
390 the transition between quantum levels i and j , the volume emis- 431
391 sion rate reaching altitude z is given by 432

$$\eta_{j \rightarrow i}^{\text{transmitted}}(z) = \eta_{j \rightarrow i}(z_0) \kappa_{j \rightarrow i}(z), \quad (12)$$

392 where $\kappa_{j \rightarrow i}(z)$ is a dimensionless attenuation factor depending 433
393 on the extinction coefficient ϵ_{ji} , the column density $\zeta_i(z, z_0)$ of 434
394 the quantum state i , and is given by

$$\kappa_{j \rightarrow i}(z) = 1 - \frac{1}{1 + 0.9948(\epsilon_{ji} \zeta_i(z, z_0))^{1.44}} \quad (13)$$

395 with

$$\epsilon_{ji} = A_{ij} \frac{2J_i + 1}{2J_j + 1} \frac{2472 \times 10^{-6} \lambda_{ij}^3}{T(z)^{0.5}}, \quad (14)$$

396 where λ_{ij} is the wavelength of the $j \rightarrow i$ transition given in cen- 437
397 timeters.

398 Thanks to this approach, self-absorbed photons are redis- 438
399 tributed to lower-energy transitions using branching ratios calcu- 439
400 lated with the appropriate Einstein factors. In addition, as most 440
401 of the continuum emission of the excited states of H₂ that we 441
402 consider in this study occurs above 120 nm, continuum self- 442
403 absorption is not taken into account in this model.

404 2.2.5. Synthetic spectrum

405 The flux $I(\lambda)$ [cm⁻²s⁻¹nm⁻¹sr⁻¹] of UV emission from the atmo- 443
406 sphere, in the θ direction, at infinite spectral resolution and with- 444
407 out taking into account absorption by hydrocarbons (Ex: CH₄, 445
408 C₂H₂, C₂H₆, ...) is given by 446

$$I(\lambda) = \frac{1}{4\pi \cos(\theta)} \int_{z_0}^{\infty} \eta_{\lambda}^{\text{tot}}(z, \lambda) dz, \quad (15)$$

409 where $\eta_{\lambda}^{\text{tot}}(z, \lambda)$ [cm⁻³s⁻¹nm⁻¹] is the total differential volume 447
410 emission rate at altitude z , which is the linear combination of 448
411 the differential volume emission rate in the continuum ($\eta_{\lambda}^{\text{cont}}(z, \lambda)$ 449
412 and the differential volume emission rate of discrete transitions 450
413 ($\eta_{\lambda}^{\text{discr}}(z, \lambda)$) in [cm⁻³s⁻¹nm⁻¹].

414 The thermal agitation of H₂ molecules having a mass m_{H_2} 451
415 leads to the discrete emission lines with a spectral broadening 452
416 defined by

$$\frac{\Delta\lambda}{\lambda} = \sqrt{\frac{2k_{\text{B}}T}{m_{\text{H}_2}c^2}}. \quad (16)$$

417 In our atmospheric model, at altitudes of around 400 km 453
418 above the cloud level (average altitude of the auroral emission 454
419 peak according to Bonfond et al. 2015) where the average tem- 455
420 perature is around 600 K (Grodent et al. 2001), the mean spectral 456
421 broadening of H₂ emission at 140 nm is around $\Delta\lambda \sim 0.002$ nm. 457
422 This Doppler broadening is well below the broadening of the in- 458
423 strumental spectral resolution. In addition, since optical depth is

very low above 400 km altitude, all spectral lines are optically 424
thin. Thus, to calculate the differential volume emission rate of 425
discrete transitions $\eta_{\lambda}^{\text{discr}}(z, \lambda)$, we used this mean Doppler broad- 426
ening for all the spectral lines considered in our model at all 427
altitudes. Thus, considering the Doppler profile $f_{\Delta\lambda}(\lambda)$ [nm⁻¹] 428
with a full width at half maximum $\Delta\lambda$ representing the mean 429
Doppler broadening in the atmospheric model used, and using 430
the volume emission rate of discrete transitions $\eta^{\text{discr}}(z, \lambda)$, we 431
have $\eta_{\lambda}^{\text{discr}}(z, \lambda) = \sum_{\lambda'} \eta^{\text{discr}}(z, \lambda') f_{\Delta\lambda}(\lambda - \lambda')$. Finally, the syn- 432
thetic spectrum $I_{\text{synth}}(\lambda)$ is calculated, taking into account the in- 433
strumental resolution $\Delta\lambda'$ with 434

$$I_{\text{synth}}(\lambda) = I(\lambda') * g_{\Delta\lambda'}(\lambda - \lambda'), \quad (17)$$

where $g_{\Delta\lambda'}(\lambda)$ is a Gaussian function with full width at half max- 435
imum $\Delta\lambda'$ and λ' is a dummy variable. 436

437 2.2.6. Hydrocarbon absorption

When magnetospheric electrons penetrate deeply enough below 438
the homopause, the emission produced by the de-excitation of 439
H₂ is attenuated at certain wavelengths by absorption from hy- 440
drocarbons. The attenuated spectral emission may be given by 441

$$I(\lambda) = \frac{1}{4\pi \cos(\theta)} \int_{z_0}^{\infty} \eta_{\lambda}^{\text{tot}}(z, \lambda) e^{-\tau^{\text{tot}}(\lambda, z)} dz, \quad (18)$$

where $\tau^{\text{tot}} = \tau_{\text{CH}_4} + \tau_{\text{C}_2\text{H}_2} + \tau_{\text{C}_2\text{H}_6} + \dots$ is the total optical depth 442
of hydrocarbons considered in the atmospheric model used; z_0 443
is the minimum altitude; and $\tau_m(z, \lambda) = \int_z^{\infty} n_m(z') \sigma_m(\lambda) dz'$ is 444
the optical depth of species m , whose number density is given 445
by $n_m(z)$, whose absorption cross section is given by $\sigma_m(\lambda)$, and 446
where z' is a dummy variable. In this study we used the cross 447
sections of CH₄ (Au et al. 1993; Kameta et al. 2002; Lee et al. 448
2001) and C₂H₂ (Cooper et al. 1995; Nakayama & Watanabe 449
2004; Wu et al. 2001) measured experimentally in the UV range. 450

451 2.2.7. Comparison with laboratory spectra and validation

To validate the H₂ UV emission model, we compared our sim- 452
ulations with experimental results from the study of Liu et al. 453
(1995). In this study the authors used a 100 eV mono-energetic 454
electron beam for bombarding H₂ molecules and measured the 455
UV emission. The spectral resolution was of about 0.0125 nm in 456
the spectral range [114 nm–170 nm]. In addition, H₂ molecules 457
with a density of $n_{\text{H}_2} = 4.55 \times 10^{12}$ cm⁻³ were placed in a cell at 458
a pressure of around 0.4 μ bar and a temperature of 300 K. 459

To validate our calculations, we compared relative spectra 460
and neglected absolute intensities between the modeled and ob- 461
served spectra in order to avoid the quantity of H₂ used in the 462
Liu et al. (1995) experiment. To do this, we considered a thin at- 463
mosphere with a temperature of 300 K, in which we precipitated 464
100 eV mono-energetic electrons (best fit A) in order to match 465
the experimental conditions of Liu et al. (1995) as faithfully as 466
possible. We then followed the same approach by precipitating 467
a Maxwellian electron (best fit B) beam with an average energy 468
of 100 eV. In Fig. 2 we represent this comparison graphically in 469
four spectral ranges (panels i to iv), each spanning 1 nm in order 470
to evaluate the differences at very high spectral resolution. 471

For the rest of the spectrum, our model is in very good 472
agreement with the experimental results. We note that the ampli- 473
tudes of some spectral lines are not perfectly reproduced by the 474

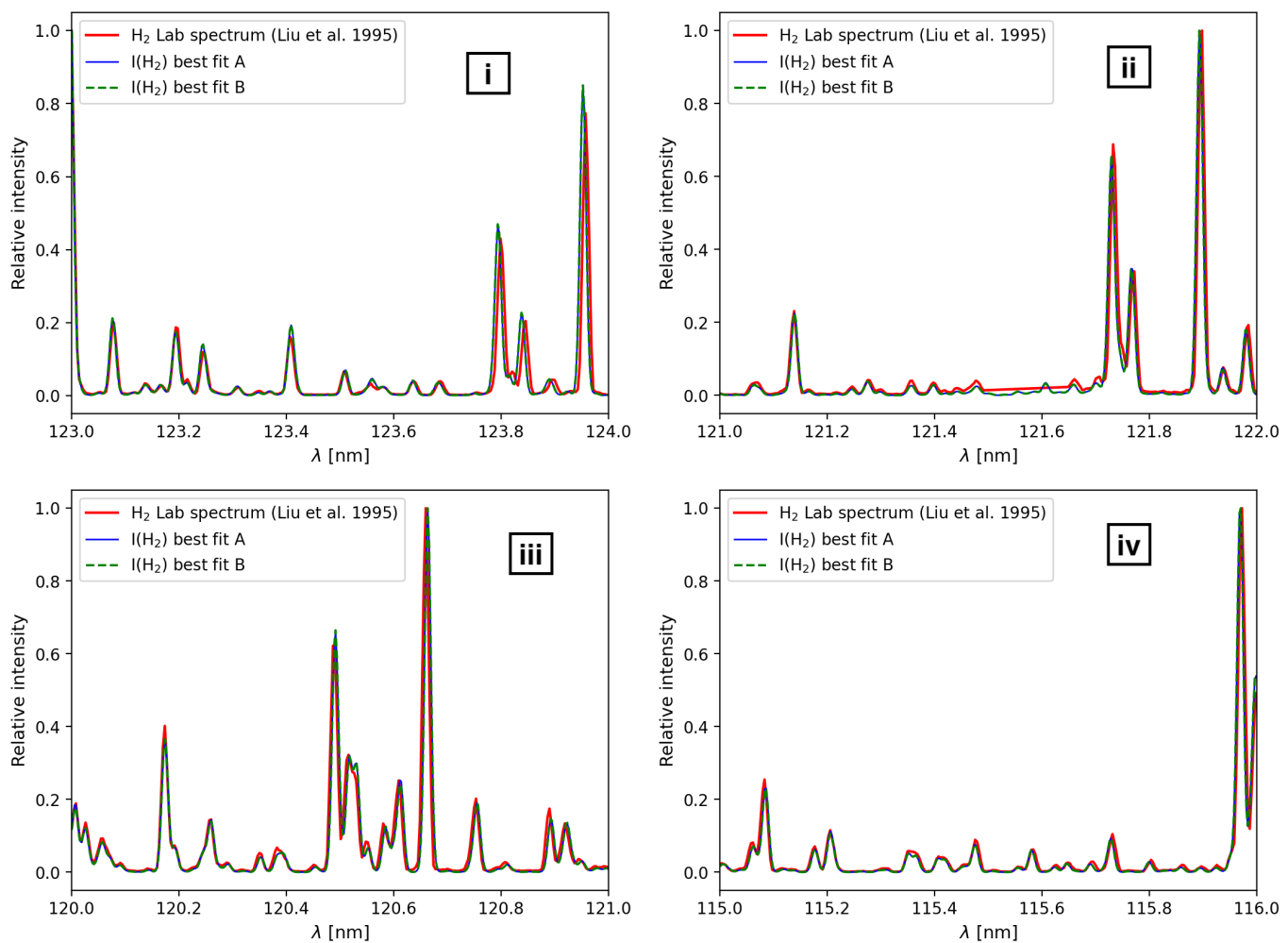


Fig. 2. Examples of comparisons of modeled synthetic spectra with experimental spectra (red line) obtained by Liu et al. (1995) with a spectral resolution of 0.0125 nm. The blue line and the dashed green line represent the best fits obtained by precipitating a 100 eV mono-energetic (best fit A) and Maxwellian (best fit B) electron flux distributions. The four spectral windows shown have a width of 1 nm. In the *ii* window around 121.567 nm, the Lyman- α line was filtered out.

475 model. These differences are minimal and are generally caused
 476 by the inhomogeneity of the electron energy spectrum exciting
 477 H₂ molecules. In reality, the incident electron beam is not per-
 478 fectly mono-energetic, and not perfectly Maxwellian either. As
 479 shown in the study by Dols et al. (2000), the variation in the
 480 energy of the electrons exciting the H₂ molecules may have a
 481 strong effect on some particular spectral lines. This influences
 482 their widths and amplitudes.

483 We also note a spectral shift of around 0.005 nm at some
 484 wavelengths between model and observation (e.g., between
 485 123.8 and 124 nm in panel *i*, between 121.7 and 122 nm in panel
 486 *ii*, and between 120.4 and 121 nm in panel *iii*). According to
 487 Dols et al. (2000), this shift is caused by thermal expansion of
 488 the structure of the spectrometer’s sensor during the measure-
 489 ments by Liu et al. (1995).

490 3. Juno/UVS observations

491 The aim of the Juno mission, launched in August 2011, is to
 492 study the planet Jupiter and its environment (Bolton et al. 2017).
 493 Its insertion into a highly elliptical polar orbit was achieved on
 494 July 5, 2016, and its first PJ was carried out on August 27, 2016.
 495 Since then the spacecraft has made several dozen PJs, with a pe-

riodicity of around 53.5 days during the nominal mission (until 496
 PJ37), leading to close flybys of the polar regions allowing us 497
 to study the interaction of the magnetosphere with the Jovian 498
 atmosphere. Juno hosts several scientific instruments, including 499
 the UltraViolet Spectrograph (UVS) (Gladstone et al. 2017). The 500
 UVS is specifically designed to study Jupiter’s atmosphere and 501
 auroral emissions in the extreme UV (EUV) and FUV domains. 502
 The wavelengths ranging from 68 nm to 210 nm are dispersed 503
 over a 256 spatial channel \times 2048 spectral channel sensor (Davis 504
 et al. 2011; Greathouse et al. 2013; Gladstone et al. 2017). The 505
 spectrometer’s slit has a dog-bone shape, and is oriented parallel 506
 to the axis of the spacecraft’s rotation. This slit has a field of view 507
 at the edges of $2.55^\circ \times 0.2^\circ$ and a spectral resolution of around 508
 1.9–3.0 nm, and a field of view at the center of $2^\circ \times 0.025^\circ$ with a 509
 spectral resolution of ~ 1.3 nm (Greathouse et al. 2013). Juno is a 510
 spin-stabilized probe with a period of about 30 s. As a result, the 511
 UVS slit is scanned across the sky to measure the UV emission 512
 spectrum in its field of view including the emission spectrum 513
 from Jupiter’s poles (Bonfond et al. 2017). Each detected photon 514
 is associated with ancillary information including (latitude, lon- 515
 gitude), x and y coordinates on the UVS detector, wavelength, 516
 emission angle from the planet. Counts recorded by UVS are 517
 converted into physical flux units using the instrument effective 518

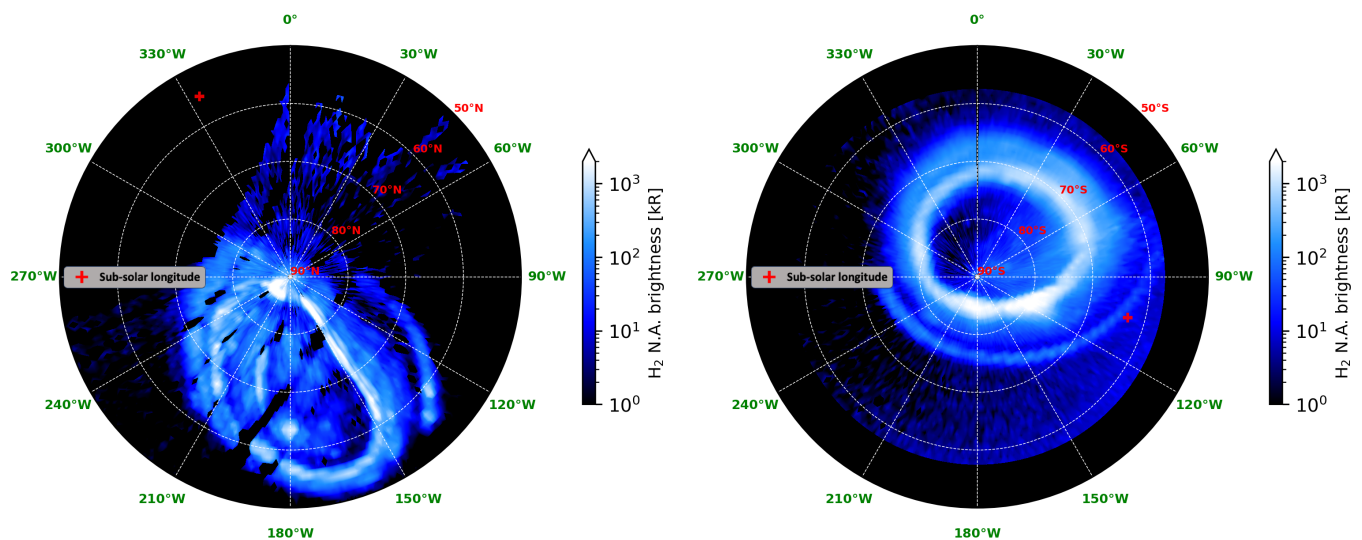


Fig. 3. Integrated non-absorbed (N.A.) UV emission from Jupiter’s auroral regions observed by Juno/UVS during PJ32 in the SIII joviocentric reference frame. The acquisition time over the northern polar region is 4,282 seconds. At the southern polar region the acquisition time is 14,561 seconds. The plus sign (+) in red represents the average solar longitude during the selected acquisition times for the northern and southern polar regions individually. Thus, the Sun’s longitudinal path between its mean position during acquisition at the northern hemisphere and the southern hemisphere is approximately 130° westward.

519 area derived from thousands of stellar observations during regu- 519
 520 lar calibration phases (Hue et al. 2019, 2021). This photon list is 520
 521 rearranged in latitude-longitude-wavelength data cubes for each 521
 522 hemisphere. Latitude and longitude is sampled every 1° and we 522
 523 used a 0.1 nm spectral sampling that fulfills the Nyquist criterion 523
 524 based on UVS spectral PSF. In addition, to increase the S/N of 524
 525 the UV emission spectra, we only map photons measured by the two 525
 526 UVS wide slits, for which the spectral resolution is around 526
 527 2.1 nm (Greathouse et al. 2013), and discarded the photons com- 527
 528 ing from the narrow slit. 528

529 For the present study we used spectral data obtained during 529
 530 PJ32, from 2021-Feb-21 16:23:09 UTC to 2021-Feb-21 530
 531 22:38:45 UTC, for a total acquisition time of 6.25 hours. This 531
 532 dataset includes 1.17 hours acquisition time for the northern pol- 532
 533 ar region and 4.04 hours for the southern polar region, with 533
 534 about 1 hour between acquisitions at the two regions (Juno’s 534
 535 passage over the equator). The acquisition time at the south pole 535
 536 is naturally longer, due to the inclination of the semimajor axis 536
 537 of Juno’s orbit to Jupiter’s equatorial plane. During each 30 sec 537
 538 spin, the UVS field of view intercepts Jupiter. Thus, each point 538
 539 on Jupiter or on the sky is looked at with an exposure of ~18 ms 539
 540 during one spacecraft spin. 540

541 Figure 3 shows the integrated non-absorbed (N.A.) UV emis- 541
 542 sion over the northern and southern polar regions. In order to iso- 542
 543 late the auroral photons from the solar emission backscattered by 543
 544 the Jovian atmosphere, we established a selection criterion for 544
 545 pixels within the aurora (see Fig. C.1). We only selected pixels 545
 546 corresponding to UV emission spectra with a signal-to-noise ratio 546
 547 (S/N) ≥ 3 . To evaluate the S/N, we consider the average of the 547
 548 unabsorbed part of the UV emission spectrum of H₂ in the spec- 548
 549 tral range [155 nm; 162 nm] to define the signal. For the noise, 549
 550 we estimated it within the same spectral range by subtracting the 550
 551 average signal value and calculating the standard deviation. 551

552 The UVS observations are co-added over the acquisition 552
 553 time into a large spectral database (latitude vs longitude vs 553
 554 wavelength), from which the CR $CR = \frac{I(155nm-162nm)}{I(125nm-130nm)}$ is then cal- 554
 555 culated, characterizing the absorption of the UV emission spec- 555
 556 trum by CH₄. It is important to note that we cannot use the ini-

557 tially defined wavelength range at the denominator (i.e., 123– 557
 558 130 nm) because of the uncertain calibration due to the detector 558
 559 degradation, which is due to gain sag on and around Lyman- α 559
 560 in the wide slit region of the detector. Hence, we start at 125 560
 561 nm instead. Polar maps of the CR in the northern and southern 561
 562 hemispheres are shown in Fig. 4. As a consequence of this differ- 562
 563 ent wavelength range, the minimum CR in these maps is about 563
 564 1.8, which is higher than the minimum CR ~ 1.1 observed by 564
 565 Gustin et al. (2013) and corresponds to an unabsorbed UV emis- 565
 566 sion spectrum. Regarding the maximum CR value, we have an 566
 567 overall $CR_{max} \approx 30$ for both poles. 567

568 4. Method

569 To map the characteristic energy of primary electrons precipitat- 569
 570 ing in auroral regions, we modeled the CR using the TransPlanet 570
 571 electronic transport model combined with the H₂ UV emission 571
 572 model. For these simulations, we considered the Grodent et al. 572
 573 (2001) atmospheric model (an atmosphere of H, H₂, He, and 573
 574 CH₄) with an altitude range from 100 km (~1 mbar) to 2300 574
 575 km ($\sim 5.3 \times 10^{-12}$ bar) above the cloud level (see Fig. 1). To sim- 575
 576 ulate the electron transport, we used two types of initial elec- 576
 577 tron flux distribution. First, we used a mono-energetic distribu- 577
 578 tion $\Phi(E, z_{max}) \sim \delta(E - E_0)$ and given by $\Phi(E, z_{max}) \sim \delta(E - E_0)$, where 578
 579 z_{max} represents the altitude at which the initial electron flux is 579
 580 injected into the atmosphere. In a second step, we used a kappa-type 580
 581 distribution $\Phi(E, z_{max}) \sim f_k(E, \langle E \rangle)$ (Coumans et al. 2002) character- 581
 582 ized by an average energy $\langle E \rangle$ and a κ parameter governing the logarith- 582
 583 mic gradient of the distribution toward high energies. The kappa 583
 584 distribution used in this study is given by 584
 585

$$585 f_k(E, \langle E \rangle) = Q_0 \frac{4 \kappa (\kappa - 1) E}{\pi (\kappa - 2)^2 \langle E \rangle} \frac{\langle E \rangle^{\kappa - 1}}{\left(\frac{2E}{\kappa - 2} + \langle E \rangle \right)^{\kappa + 1}}, \quad (19)$$

586 where Q_0 is the total energy flux and $\langle E \rangle$ is given as a function 586
 587 of the characteristic energy E_0 by the expression $\langle E \rangle = 2E_0 \frac{\kappa}{\kappa - 2}$, 587

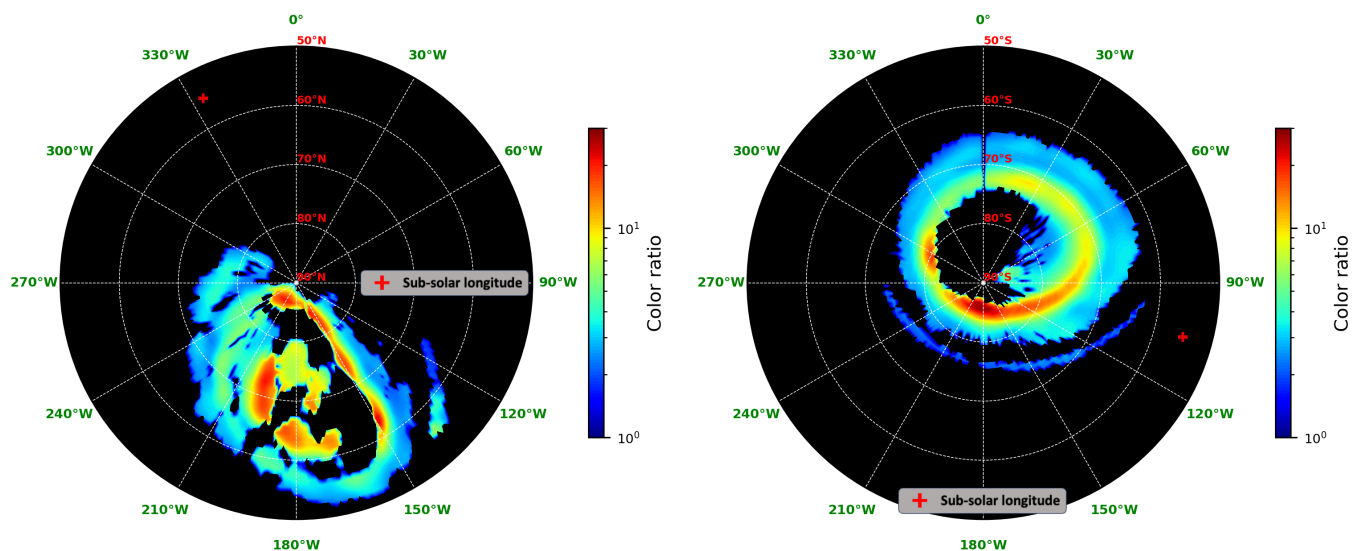


Fig. 4. Color ratio of Jupiter’s auroral regions (left: northern hemisphere; right: southern hemisphere) observed during PJ32. The panels show the CR calculated for each pixel of the UV emission map as defined by Gustin et al. (2016) with $CR = \frac{I(155nm-162nm)}{I(125nm-130nm)}$.

588 with E_0 representing the energy of the maximum amplitude of the
589 distribution.

590 In Fig. 5 we give some examples of kappa electron flux distributions.
591 Unlike the Maxwellian distributions used in previous
592 electron transport models (e.g., Gustin et al. 2016), this distribu-
593 tion extends to higher energies. The value of kappa ($\kappa = 2.5$) that
594 controls the amplitude of the distribution toward high energies
595 and that we use in this study was derived from observed electron
596 fluxes by Juno/JEDI during the first 20 PJs (Salveter et al. 2022).
597 Hence, this kappa value gives rise to a realistic distribution of
598 electron energy flux precipitating in Jupiter’s auroral regions.

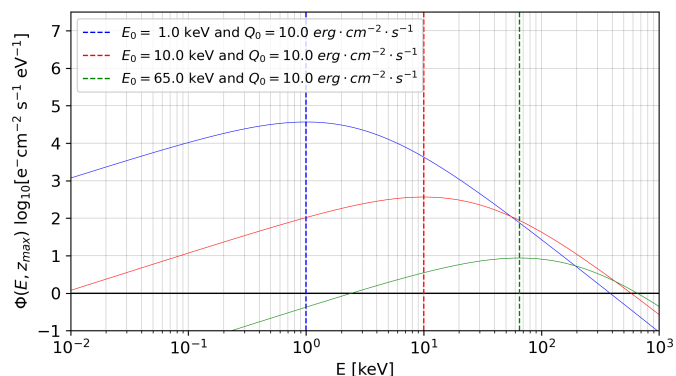


Fig. 5. Examples of kappa distributions with different characteristic energies. The three examples use $\kappa = 2.5$ and $Q_0 = 10 \text{ erg}\cdot\text{cm}^{-2}\cdot\text{s}^{-1}$, and three different characteristic energies: $E_0 = 1 \text{ keV}$, $E_0 = 10 \text{ keV}$, and $E_0 = 65 \text{ keV}$.

599 After modeling the electron transport, the resulting $\Phi(E, z)$
600 electron flux is used to calculate the excitation rates of H_2 be-
601 fore simulating the atmospheric spectral emission in a given θ
602 direction. Depending on the characteristic energy of the initial
603 precipitated electron flux distributions, the electrons penetrate to
604 varying depths into the atmosphere. As a result, the UV spectral
605 emission of H_2 is absorbed to varying degrees by hydrocarbons
606 below the homopause.

607 In the UV emission model, we considered absorption by
608 CH_4 , which absorbs mainly below 140 nm (see Fig. 6 for the

optical depth of CH_4 and C_2H_2). We also included absorption by 609
610 C_2H_2 , whose distribution profile is shown in Fig. 1. This second
611 hydrocarbon absorbs mainly in the spectral range [150 nm–153
612 nm] and in other small ranges below 140 nm (see Fig. 6). This
613 means that longward of 145 nm, only C_2H_2 can attenuate the
614 UV emission spectrum. However, short of this wavelength, CH_4
615 is the major absorber and C_2H_2 has a weak influence on the am-
616 plitude of the UV spectrum.

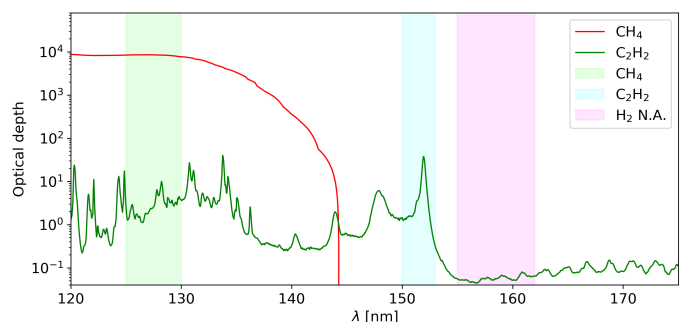


Fig. 6. Optical depth calculated over the atmospheric column for CH_4
and C_2H_2 . The transparent green and cyan bands represent the absorp-
tion spectral ranges used for the CR calculations. For CH_4 the absorp-
tion spectral range is considered between 125 nm and 130 nm and for
 C_2H_2 between 150 nm and 153 nm. The transparent magenta band is the
non-absorbed (N.A.) spectral range over which hydrocarbon absorption
was assumed to be negligible.

617 During PJ32, the close flyby of Jupiter’s poles is such that 617
618 each point in both polar zones (north or south) is observed with a
619 different viewing angle. Accordingly, each spectrum is measured
620 with a different median θ emission angle (see Fig. C.2).

621 In the next step, for each characteristic energy, we modeled
622 the spectral emission with a spectral resolution of 2.1 nm (com-
623 parable to UVS spectra), varying the emission angle between 0°
624 and 80° . This allowed us to establish the relationship $CR(E_0, \theta)$,
625 which links the CR, the emission angle, and the characteristic en-
626 ergy of the initial electron flux distribution injected at the top of
627 the modeled atmosphere. With the assumption that the $CR(E_0, \theta)$
628 function is monotonic, we could then invert this relationship to

629 calculate E_0 using the CR observed by UVS and the emission
630 angle maps.

631 In this study we distinguished the $\text{CR}(E_0, \theta)$ relationship in
632 the northern and southern hemispheres according to the mag-
633 netic dip angle in these auroral regions (see Appendix D.1).
634 Thus, for each type of electron flux distribution and for each
635 polar region, the relationship $\text{CR}(E_0, \theta)$ is modeled and fitted⁵
636 using the formula D.2 (see Appendix D.2). For the case of mono-
637 energetic initial electron flux distribution, the $\text{CR}(E_0, \theta)$ relation-
638 ship we modeled is shown in gold in the left panel of Fig. D.2
639 for the north pole, and separately in the left panel of Fig. D.3
640 for the south pole. In these same figures, we plot the fit of the rela-
641 tionship $\text{CR}(E_0, \theta)$ in green grid lines,⁶ and we evaluated the un-
642 certainty of this fit by plotting the absolute differences between
643 the fit and the model for the north and south poles. The mean
644 absolute difference is around 0.6, which is comparable to the un-
645 certainty of the $\text{CR}(E_0, \theta)$ relationship that we modeled for the
646 case of the mono-energetic distribution (see Table D.1).

647 For the case of the kappa distribution, the results are shown
648 in the right panel of Fig. D.2 for the north pole and in the right
649 panel of Fig. D.3 for the south pole, using the same conven-
650 tions. The average absolute difference between fits and mod-
651 els is around 0.5, which is comparable to the uncertainty of the
652 modeled $\text{CR}(E_0, \theta)$ relationship in this case. Whatever the initial
653 electron flux distribution, our results shows that neglecting the
654 emission angle leads to an underestimation of the characteristic
655 energy.

656 5. Results and discussion

657 In comparison with the $\text{CR}(E_0)$ relationship modeled by Gustin
658 et al. (2016) by precipitating a Maxwellian electron flux, our re-
659 sults show that the CR increases about two times faster in the
660 case of a mono-energetic distribution. In their model, Gérard
661 et al. (2014) also modeled the $\text{CR}(E_0)$ relationship when pre-
662 cipitating mono-energetic electron fluxes. For a fixed θ emis-
663 sion angle, our results show that the CR increases about three
664 times faster than that of Gérard et al. (2014). This can be ex-
665 plained by the fact that the modeling of auroral spectral emission
666 in these previous studies is different from our case. In our UV
667 emission model we calculate the volume emission rate (VER)
668 by considering all the excitation rates of all the rovibrational
669 levels (v, J) of the H_2 electronic states that we take into ac-
670 count. However, in the studies by Gérard et al. (2014) and Gustin
671 et al. (2016), the UV emission of H_2 molecules is modeled us-
672 ing the volume emission rate (VER) obtained directly from the
673 cross sections of the interactions $e^- + \text{H}_2 \rightarrow e^- + \text{H}_2^*(B^1\Sigma_u^+)$ and
674 $e^- + \text{H}_2 \rightarrow e^- + \text{H}_2^*(C^1\Pi_u)$ measured by Dalgarno et al. (1999).
675 The unabsorbed spectrum is obtained by multiplying the VER by
676 a synthetic spectrum of H_2 (see Eq. 6 in Gustin et al. 2016). The
677 absorbed spectrum is calculated taking into account the abun-
678 dance of hydrocarbons in the atmosphere in the same way as ex-
679 plained previously. Thus, the differences in calculated CRs are
680 mainly due to very small differences in the VER peak altitude
681 obtained from these different studies. In addition, the electronic
682 transport model used in these previous studies is based on Monte
683 Carlo simulations. Compared with our transport model, which
684 uses a radiative transfer solver, this could introduce additional

685 discrepancies in the results. In comparison with the studies that
686 modeled the $\text{CR}(E_0)$ relationship, we still have a monotonically
687 increasing CR as a function of characteristic energy.

688 5.1. Mapping the characteristic energy using the 689 mono-energetic initial distribution of the electron flux

690 Using the modeled $\text{CR}(E_0, \theta)$ relationship (shown in Figures D.2
691 and D.3), we inverted Equation D.2 to determine $E_0(\text{CR}, \theta)$. We
692 obtained characteristic energy maps E_0 from the observed PJ32
693 CR and emission angle maps shown in Figures 4 and C.2, res-
694 pectively.

695 Figure 7 shows the resulting characteristic energy maps for
696 the mono-energetic case in the northern (left panel of Fig. 7) and
697 southern (right panel of Fig. 7) auroral regions. The average es-
698 timated uncertainty on the characteristic energy is derived from
699 the average uncertainty on the $\text{CR}(E_0, \theta)$ modeling presented in
700 table D.1. For the mono-energetic distribution, it is around 6 keV
701 for both auroral regions. At the north pole the estimated maxi-
702 mum characteristic energy is around (150 ± 6) keV in the polar
703 emission region. There are also other peaks with characteristic
704 energies of up to (120 ± 6) keV in the injection zone of the
705 main emission region near the pole. For the south pole the es-
706 timated maximum characteristic energy is around (170 ± 6) keV
707 in the main emission region, with secondary peaks ranging from
708 (90 ± 6) keV to (150 ± 6) keV and spread throughout the auroral
709 arc.

710 In the polar emission zone the characteristic energy is low,
711 with a peak of around (60 ± 6) keV. During PJ32 the region of
712 polar emission in the south was not very bright. This may be due
713 to exceptionally low-energy electron precipitation or it could be
714 due to exceptionally low electron flux in general, which does
715 not produce strong UV emission. For other PJs (e.g., PJ4, PJ5,
716 PJ8, PJ13, PJ14), the polar emission region in the south pole was
717 relatively bright, and its spectral emission was largely detectable
718 by UVS (Greathouse et al. 2021).

719 We also observed that there is no similarity between the char-
720 acteristic energies of the auroral regions connected by the mag-
721 netic field lines between the north and south poles. This seems, at
722 first order, to indicate a different electronic precipitation between
723 the two auroral regions. However, the overall range of energies
724 along the auroral ovals appears to be similar.

725 In our modeling of the $\text{CR}(E_0, \theta)$ relationship we did not take
726 into account the width of the horizontal extension of the auroral
727 emission resulting from main emissions and Io's magnetic foot-
728 print (Bonfond et al. 2009). Thus, the energies inferred in the
729 very narrow regions bordering the auroral ovals are not usable.
730 In consequence, the results presented here are not valid for the Io
731 footprint region. In addition, we did not take into account the SIII
732 longitudinal motion of Io's footprint during the acquisition times
733 in the northern and southern auroral regions. This could signifi-
734 cantly decrease the emission and the CR of Io's footprint. Fur-
735 thermore, according to Bonfond (2010), the average energies of
736 electrons precipitating in this region are around 1–2 keV, which,
737 according to our model, cannot be detected. For electrons with
738 energies below 5 keV, the CR ratio produced is minimal because
739 they cannot penetrate deeply enough below the CH_4 homopause.

740 5.2. Mapping the characteristic energy using kappa initial 741 distribution of the electron flux

742 In the same way as for the case of the mono-energetic distribu-
743 tion, we also derived characteristic energy maps for kappa distri-

⁵ The fitting procedure is detailed in Appendix D.2.

⁶ In Figs. D.2 and D.3, the green grid lines representing the fit of the relationship $\text{CR}(E_0, \theta)$ is calculated using the parameters obtained by Markov chain Monte Carlo (MCMC) fitting in Table D.1 for each case by using the relationship D.2.

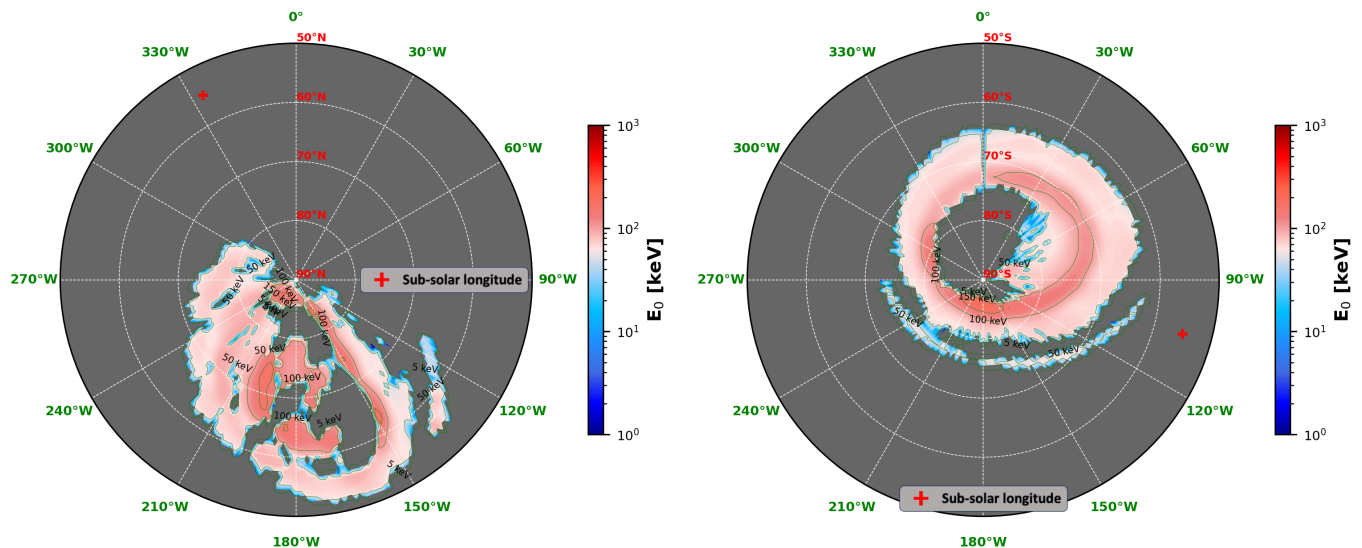


Fig. 7. Characteristic energy maps E_0 obtained from the $CR(E_0, \theta)$ relationships (see Figures D.2 and D.3) modeled for the case of an initial mono-energetic electron flux distribution, and from the CR observed during PJ32, at the north (left panel) and south (right panel) poles. Iso-energy lines are defined for values of 1 keV, 5 keV, 10 keV, in steps of 20 keV between 10 keV and 300 keV, and then in steps of 100 keV between 300 and 900 keV.

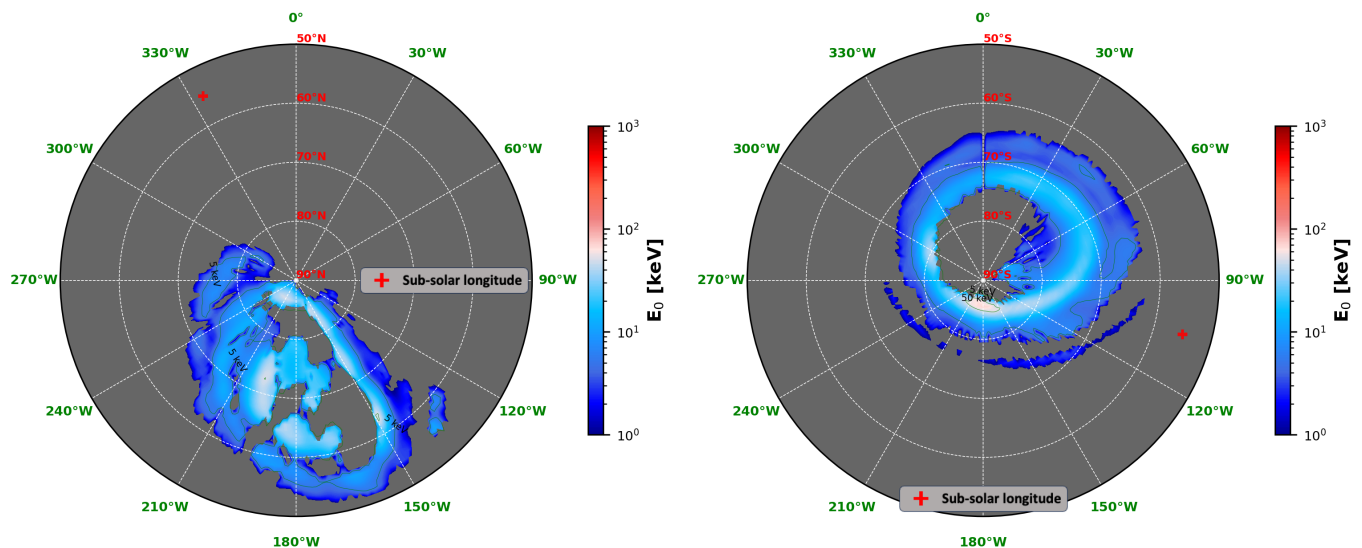


Fig. 8. Characteristic energy maps E_0 obtained from the $CR(E_0, \theta)$ relations (see Figs. D.2 and D.3) modeled for the case of an initial kappa electron flux distribution, and from the CR observed during PJ32, at the north (left panel) and south (right panel) poles. Iso-energy lines are defined in the same way as in Fig. 7.

744 butions of electrons precipitating in the auroral regions. Figure
 745 8 displays the characteristic energy maps for the northern and
 746 southern polar regions (left and right panels of Fig. 8, respec-
 747 tively). The mean energy uncertainty of these maps is estimated
 748 around 4 keV for both auroral regions. At the north pole the
 749 maximum characteristic energy is around (40 ± 4) keV in the
 750 polar emission region. In the main emission regions we obtained
 751 a maximum characteristic energy of around (10 ± 4) keV. At the
 752 south pole we obtained peaks between 30 and 50 keV in the main
 753 emission oval.

754 The characteristic energy maps in Figures 7 and 8 cannot be
 755 directly compared. In the case of a mono-energetic distribution,
 756 the characteristic energy is identical to the average energy of the
 757 distribution, whereas for the kappa distribution E_0 represents the
 758 energy of the distribution peak. In the energy maps shown in

759 Fig. 8, each pixel represents a kappa distribution described by
 760 a characteristic energy E_0 and a parameter $\kappa = 2.5$. Therefore,
 761 only the average energy of the kappa distribution can be used
 762 for comparison with a mono-energetic distribution. For a Kappa
 763 distribution, the conversion from characteristic energy to mean
 764 energy can be obtained from the relation $\langle E \rangle = 2E_0 \frac{\kappa}{\kappa-2}$.

765 Figure 9 represents the corresponding mean energy maps of
 766 electrons precipitating in the auroral regions for the case of a
 767 kappa distribution in the north (left panel of Fig. 8) and in the
 768 south (right panel of Fig. 8). The mean energy $\langle E \rangle$ being propor-
 769 tional to $2 \frac{\kappa}{\kappa-2}$, for a parameter $\kappa = 2.5$ its value is therefore ten
 770 times larger than the characteristic energy. The uncertainty on
 771 the energies is also ten times larger. Comparison with the maps in
 772 Fig. 7 shows that the spatially averaged mean energy of electrons
 773 precipitating in auroral regions is significantly underestimated

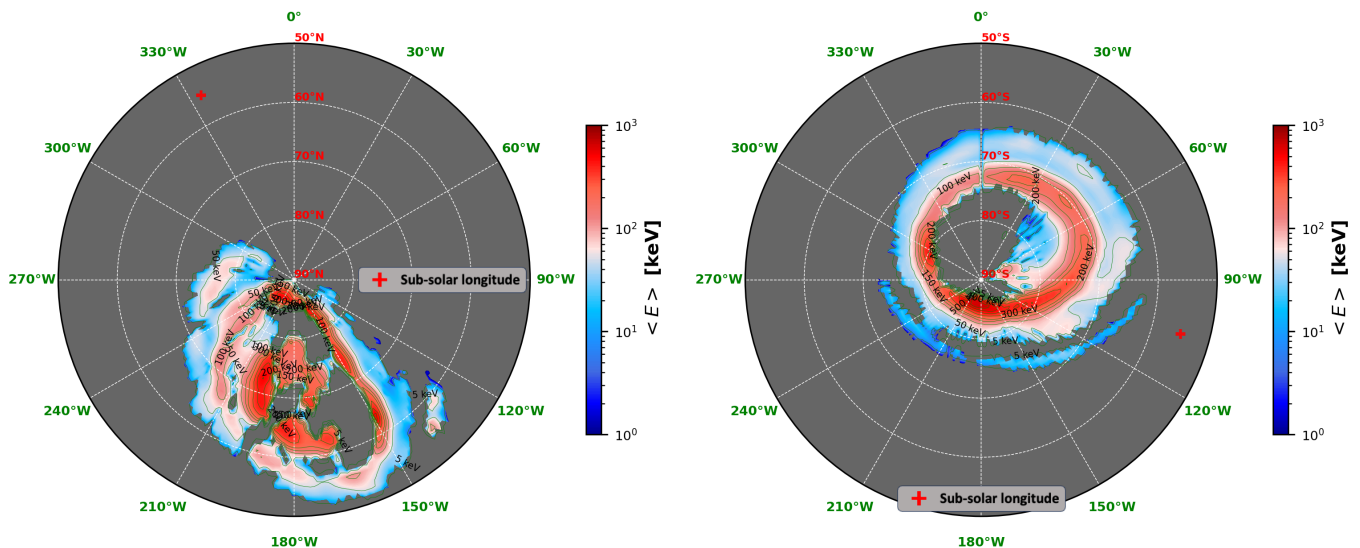


Fig. 9. Maps of the average energy $\langle E \rangle$ defined in Eq. 19 and given by the formula $\langle E \rangle = 2E_0 \frac{\kappa}{\kappa+2}$. These maps are calculated for the north (left panel) and south (right panel) poles directly from the maps in Fig. 8. The iso-energy lines are defined as for Figures 7 and 8 and with the same color bar normalization.

774 when the $CR(E_0, \theta)$ relationship is modeled by mono-energetic
 775 distributions. However, for a fixed emission angle ($\theta = 0^\circ$) we
 776 compared the $CR(\langle E \rangle)$ relationship, at low energies, between the
 777 two cases of electron flux distribution precipitating in auroral
 778 regions (see panel *c* in Fig. D.4). We found that the $CR(\langle E \rangle)$
 779 relationship obtained for the case of a mono-energetic distribution
 780 overestimates the mean electron energy below $\langle E \rangle = 90$ keV.
 781 Above 90 keV, the energy of precipitating electrons is under-
 782 estimated by the mono-energetic distribution assumption. This
 783 value of $\langle E \rangle = 90$ keV, which represents the intersection between
 784 the two $CR(\langle E \rangle)$ relationships (obtained for the case of a mono-
 785 energetic electron flux distribution and for the case of a kappa
 786 distribution), seems to be linked to the atmospheric model used
 787 and particularly to the CH_4 homopause considered (see panel *c*
 788 in Fig. D.4).

789 Previous studies that modeled the relationship between the
 790 mean energy of precipitating electrons and CR in Jupiter's auroral
 791 regions obtained mean energy maps that differ from our results.
 792 In the case of Gérard et al. (2014), the mean-energy maps
 793 were based on HST observations from January 2014 and consid-
 794 ered mono-energetic distributions of electrons precipitating
 795 in the atmospheric model described by Grodent et al. (2001).
 796 Gérard et al. (2014) obtained mean energy peaks of up to 500
 797 keV in the northern polar emission region, which is comparable
 798 to the energy peaks we obtained in the case of a kappa distribu-
 799 tion (see Fig. 9). However, this agreement should be qualified by
 800 the fact that these observations were obtained almost ten years
 801 apart and may be very different. Moreover, auroral fluctuations
 802 in UV-auroral emission brightness can be significant even over
 803 relatively short periods of time. Similarly, the Gustin et al. (2016)
 804 energy measurements cannot be directly compared with our results
 805 since they used observations obtained several years after
 806 PJ32.

807 Furthermore, we compared the average energies obtained in
 808 our study with the in situ measurements conducted by Mauk
 809 et al. (2020) using the JEDI instrument during PJs 4, 6, 7, and
 810 10 of the Juno mission. However, the JEDI measurements by
 811 Mauk et al. (2020) for each PJ cover only a minimal fraction of
 812 the polar regions associated with the intersection of Juno's foot-
 813 print and the auroral emission oval in the northern and southern

auroral regions. We evaluated that the average energies of elec-
 814 trons precipitating in these auroral regions, measured by JEDI at
 815 Juno's altitudes, range between 150 and 300 keV. In comparison
 816 with the results of our study, where we consider kappa distribu-
 817 tions for precipitating electrons, we observe energies distributed
 818 between 100 and 200 keV in approximately 70% of the auroral
 819 region (either north or south), with peaks reaching up to 600 keV
 820 in the remainder of these zones. Thus, the mean energies derived
 821 at auroral altitudes are generally of the same order as the
 822 results obtained by Mauk et al. (2020). However, at this stage, it is
 823 premature to draw a definitive conclusion regarding the compar-
 824 ison between our results and the measurements of electron en-
 825 ergy distributions conducted by Mauk et al. (2020). The auroral
 826 emission maps used to derive the mean energies of precipitating
 827 electrons are integrated over several hours, whereas JEDI mea-
 828 surements are almost instantaneous. Moreover, given the rapid
 829 dynamics of polar regions, including phenomena like short-lived
 830 bright flares and local temporal variations, it is challenging to go
 831 beyond a comparison of orders of magnitude. This comparison
 832 thus requires a more in-depth analysis, which will be the subject
 833 of further study.
 834

835 In the present study, and in previous similar studies (e.g.,
 836 Trafton et al. 1994, 1998; Gustin et al. 2002; Ajello et al. 2005;
 837 Gérard et al. 2014; Gustin et al. 2016), the $CR(\langle E \rangle)$ relationship
 838 is modeled by considering a 1D atmosphere model assuming a
 839 constant homopause throughout the auroral regions, which is a
 840 very approximate hypothesis. Hydrocarbon abundances in auro-
 841 ral regions are expected to be influenced by the precipitation of
 842 magnetospheric charged particles. Recent observations of these
 843 abundances (e.g., Sinclair et al. 2018) demonstrate that the spa-
 844 tial distribution of the main hydrocarbons in the auroral region is
 845 inhomogeneous. The maximum molar fraction variability factor
 846 in the auroral region is around 1.2 for C_2H_2 , 1.1 for C_2H_6 , and up
 847 to 1.3 for C_2H_4 at 0.01 mbar pressure only in the north pole (see
 848 Sinclair et al. 2018). For the southern auroral region the variabil-
 849 ity is also significant, and differs from that of the north. As CH_4
 850 photolysis is one of the sources of production of these different
 851 hydrocarbons, this suggests that the altitude of its homopause is
 852 also variable in the auroral regions. This may impact the esti-
 853 mates of the average energy of electrons precipitating in these

regions. To evaluate this impact, we modeled the $CR(\langle E \rangle)$ relationship using two different CH_4 abundance profiles based on the A and C eddy diffusion models of Moses et al. (2005) and Hue et al. (2018). These profiles are not representative of CH_4 auroral abundance, but have a higher homopause compared with the atmospheric model of Grodent et al. (2001) (see panel *a* in Fig. D.4). Using this approach, the results obtained (Fig. D.4 shown in Appendix D.3) suggest that, depending on the CH_4 abundance profile used in our atmospheric model, the $CR(\langle E \rangle)$ relationship increases more rapidly or less rapidly as a function of $\langle E \rangle$, as shown in Fig. D.4. The consequences of this variability for the average energy map determination may also be significant. However, this issue is beyond the scope of this article, and is left to a future investigation.

6. Conclusions

The present study is a further step forward in the investigation of electron energies precipitating in Jupiter’s auroral regions. Inspired by Dols et al. (2000), Gustin et al. (2002) and Menager (2011), we developed a new model of UV emission from H_2 in Jupiter’s auroral regions and adapted it to Juno/UVS observations. This model is more complete than previous studies. It takes into account nine electronic states of the H_2 molecule, and we combined it with the TransPlanet electronic transport model (Stamnes & Rees 1983b; Simon et al. 2007; Gronoff 2009; Menager 2011; Benmahi 2022). The H_2 auroral emission model was validated by simulating UV emission spectra at very high spectral resolution and comparing it with the results of Liu et al. (1995). The modeled UV spectra between 125 nm and 170 nm are compared with some of the emission spectra observed by UVS. The fit results are in good agreement with the observations (see Figures B.1 and B.2 in Appendix B) except in the wavelength range between 140 nm and 150 nm where the modeled spectra are more intense because we only take into account absorption by CH_4 and C_2H_2 . Between 150 and 153 nm, absorption by C_2H_2 is not strong enough for a good fit of the UVS spectra shown in Figures B.1 and B.2. This suggests that the C_2H_2 abundance profile we used in this study is underestimated in Jupiter’s auroral regions. We did not include absorption by C_2H_6 because we do not have an auroral abundance profile for this chemical species. However, as demonstrated in Gustin et al. (2016), C_2H_6 absorbs in the interval [140 nm–150 nm] and influences the amplitude of the spectrum when electrons reach the homopause, typically for average energies above 20 keV.

Thanks to Juno/UVS observations during PJ32, we mapped the CR at the north and south polar regions and used them to map the energy of precipitating primary electrons. The relationship $CR(E_0, \theta)$ was modeled taking into account the emission angle at each observed point in both auroral regions. We used the atmosphere model of Grodent et al. (2001) and considered a constant homopause throughout the auroral regions.

In the northern and southern auroral regions, using the JRM33 magnetic field model (Connerney et al. 2022), we found that the magnetic dip angle varies between $\psi \sim 60^\circ$ and $\psi \sim 80^\circ$. As the penetration depth of electrons precipitating in these regions is influenced by the magnetic dip angle, this has an impact on the CR. We modeled the $CR(E_0)$ relationship for small variations in ψ and found a small influence. This allowed us to consider only the median value of ψ in each auroral region for our modeling, in order to distinguish between the modeling of the $CR(E_0)$ relationship in the north and south.

Modeling of the $CR(E_0, \theta)$ relationship was carried out by considering mono-energetic initial electron flux distribution and

kappa distribution ($\kappa = 2.5$). This allowed us to compare results from previous works to those obtained with a more realistic broadband population. We found that when considering a mono-energetic distribution, the average energy of electrons precipitating in auroral regions is globally underestimated by a factor of 3 to 4. We also found that at low energies (below ~ 100 keV), the $CR(\langle E \rangle)$ relationships intersect (see panel *c* in Fig. D.4). Thus, below $\langle E \rangle = 90$ keV, the average electron energy is overestimated if the mono-energetic hypothesis is used to infer the mean energy of a broadband population. Above 90 keV, the energy of electrons precipitating into auroral regions is underestimated.

Our results clearly demonstrate the importance of considering broadband distributions representative of the actual particle observations (e.g., Salveter et al. 2022) and modeled here as a kappa distribution when modeling the CR relationship as a function of the average energy of electrons precipitating in auroral regions. The average energies inferred by this method under the above-mentioned hypotheses for the atmospheric composition profile lie in the 300–500 keV range in the polar emission region of the north. In the main emission zones we found average energies up to 550 keV, with peaks along the auroral oval. In the outer emission regions the average energies lie between 5 and 50 keV. In the south the polar emissions are much fainter (see also Greathouse et al. 2021) with a mean energy peak of about 100 keV. In the main emission regions we found several average energy peaks from 150 keV to 600 keV.

Finally, thanks to this study, our work can be readily applied to mapping the average energy of auroral electrons for all Juno mission PJs. This will allow us to establish a temporal map of the electron energies precipitating in these regions. We also aim to improve this study by taking into account the meridional and latitudinal variabilities of the CH_4 homopause.

Acknowledgements. This work was supported by the University of Liege under Special Funds for Research, IPD-STEMA Programme. CSW thanks the Austrian Science Fund (FWF) and project P35954-N. VH acknowledges support from the French government under the France 2030 investment plan, as part of the Initiative d’Excellence d’Aix-Marseille Université – A*MIDEX AMX-22-CPJ-04.

References

- Abgrall, H., Roueff, E., Launay, F., & Roncin, J.-Y. 1994, *Canadian Journal of Physics*, 72, 856, publisher: NRC Research Press
- Abgrall, H., Roueff, E., Liu, X., & Shemansky, D. E. 1997, *The Astrophysical Journal*, 481, 557, publisher: IOP Publishing
- Abgrall, H., Roueff, E., Liu, X., Shemansky, D. E., & James, G. K. 1999, *Journal of Physics B: Atomic, Molecular and Optical Physics*, 32, 3813
- Ajello, J. M., Pryor, W., Esposito, L., et al. 2005, *Icarus*, 178, 327
- Au, J. W., Cooper, G., Burton, G. R., Olney, T. N., & Brion, C. E. 1993, *Chemical Physics*, 173, 209
- Benmahi, B. 2022, Phd thesis, Université de Bordeaux, thesis in Astrophysics Plasmas and Nuclearphysics
- Blelly, P. L., Robineau, A., & Alcaide, D. 1996, *Journal of Atmospheric and Terrestrial Physics*, 58, 273, aDS Bibcode: 1996JATP...58..273B
- Bolton, S. J., Adriani, A., Adumitroaie, V., et al. 2017, *Science*, 356, 821
- Bonfond, B. 2010, *Journal of Geophysical Research: Space Physics*, 115, _eprint: <https://onlinelibrary.wiley.com/doi/pdf/10.1029/2010JA015475>
- Bonfond, B., Gladstone, G. R., Grodent, D., et al. 2017, *Geophysical Research Letters*, 44, 4463, _eprint: <https://onlinelibrary.wiley.com/doi/pdf/10.1002/2017GL073114>
- Bonfond, B., Grodent, D., Gérard, J.-C., et al. 2009, *Journal of Geophysical Research: Space Physics*, 114, _eprint: <https://onlinelibrary.wiley.com/doi/pdf/10.1029/2009JA014312>
- Bonfond, B., Gustin, J., Gérard, J.-C., et al. 2015, *Annales Geophysicae*, 33, 1211, publisher: Copernicus GmbH
- Broadfoot, A. L., Belton, M. J. S., Takacs, P. Z., et al. 1979, *Science*, 204, 979, publisher: American Association for the Advancement of Science
- Clark, G., Mauk, B. H., Haggerty, D., et al. 2017, *Geophysical Research Letters*, 44, 8703, _eprint: <https://onlinelibrary.wiley.com/doi/pdf/10.1002/2017GL074366>

- 984 Clarke, J. T., Ballester, G., Trauger, J., et al. 1998, *Journal of Geophysical Research: Planets*, 103, 20217, [_eprint: https://onlinelibrary.wiley.com/doi/pdf/10.1029/98JE01130](https://onlinelibrary.wiley.com/doi/pdf/10.1029/98JE01130)
- 985
- 986
- 987 Clarke, J. T., Ballester, G. E., Trauger, J., et al. 1996, *Science*, 274, 404, publisher: American Association for the Advancement of Science
- 988
- 989 Clarke, J. T., Moos, H. W., Atreya, S. K., & Lane, A. L. 1980, *The Astrophysical Journal*, 241, L179, aDS Bibcode: 1980ApJ...241L.179C
- 990
- 991 Connerney, J. E. P., Timmins, S., Oliverson, R. J., et al. 2022, *Journal of Geophysical Research: Planets*, 127, e2021JE007055, number: 2 [_eprint: https://onlinelibrary.wiley.com/doi/pdf/10.1029/2021JE007055](https://onlinelibrary.wiley.com/doi/pdf/10.1029/2021JE007055)
- 992
- 993
- 994 Cooper, G., Burton, G. R., & Brion, C. E. 1995, *Journal of Electron Spectroscopy and Related Phenomena*, 73, 139
- 995
- 996 Coumans, V., Gérard, J.-C., Hubert, B., & Evans, D. S. 2002, *Journal of Geophysical Research: Space Physics*, 107, S1A 5, [_eprint: https://onlinelibrary.wiley.com/doi/pdf/10.1029/2001JA009233](https://onlinelibrary.wiley.com/doi/pdf/10.1029/2001JA009233)
- 997
- 998
- 999 Dalgarno, A., Yan, M., & Liu, W. 1999, *The Astrophysical Journal Supplement Series*, 125, 237, publisher: IOP Publishing
- 1000
- 1001 Davies, D. K., Kline, L. E., & Bies, W. E. 1989, *Journal of Applied Physics*, 65, 3311
- 1002
- 1003 Davis, M. W., Gladstone, G. R., Greathouse, T. K., et al. 2011, in *Radiometric performance results of the Juno ultraviolet spectrograph (Juno/UVS)*, ed. H. A. MacEwen & J. B. Breckinridge, San Diego, California, USA, 814604
- 1004
- 1005
- 1006 Dols, V., Gérard, J. C., Clarke, J. T., Gustin, J., & Grodent, D. 2000, *Icarus*, 147, 251
- 1007
- 1008 Dols, V., Gérard, J. C., Paresce, F., Prangé, R., & Vidal-Madjar, A. 1992, *Geophysical Research Letters*, 19, 1803, [_eprint: https://onlinelibrary.wiley.com/doi/pdf/10.1029/92GL02104](https://onlinelibrary.wiley.com/doi/pdf/10.1029/92GL02104)
- 1009
- 1010
- 1011 Elliott, S. S., Gurnett, D. A., Kurth, W. S., et al. 2018, *Journal of Geophysical Research: Space Physics*, 123, 7523, [_eprint: https://onlinelibrary.wiley.com/doi/pdf/10.1029/2018JA025797](https://onlinelibrary.wiley.com/doi/pdf/10.1029/2018JA025797)
- 1012
- 1013
- 1014 Foreman-Mackey, D., Hogg, D. W., Lang, D., & Goodman, J. 2013, *Publications of the Astronomical Society of the Pacific*, 125, 306, number: 925 arXiv: 1202.3665
- 1015
- 1016
- 1017 Gladstone, G. R., Persyn, S. C., Eterno, J. S., et al. 2017, *ssr*, 213, 447
- 1018
- 1019
- 1020 Gladstone, G. R. & Skinner, T. E. 1989, *NASA Special Publication*, 494, 221, aDS Bibcode: 1989NASSP.494..221G
- 1021
- 1022
- 1023 Greathouse, T., Gladstone, G. R., Versteeg, M., et al. 2021, *Journal of Geophysical Research: Planets*, 126, e2021JE006954, [_eprint: https://onlinelibrary.wiley.com/doi/pdf/10.1029/2021JE006954](https://onlinelibrary.wiley.com/doi/pdf/10.1029/2021JE006954)
- 1024
- 1025
- 1026 Greathouse, T. K., Gladstone, G. R., Davis, M. W., et al. 2013, in *UV, X-Ray, and Gamma-Ray Space Instrumentation for Astronomy XVIII*, Vol. 8859 (SPIE), 216–226
- 1027
- 1028
- 1029 Grodent, D. 2015, *Space Science Reviews*, 187, 23
- 1030
- 1031
- 1032 Grodent, D., Gladstone, G. R., Gérard, J. C., Dols, V., & Waite, J. H. 1997, *Icarus*, 128, 306
- 1033
- 1034 Grodent, D., Waite, J. H., & Gérard, J.-C. 2001, *J. Geophys. Res.*, 106, 12933
- 1035
- 1036
- 1037 Gronoff, G. 2009, PhD thesis, thèse de doctorat dirigée par Liliensten, Jean Astrophysique et milieux dilués Grenoble 1 2009
- 1038
- 1039
- 1040 Gronoff, G., Hegyi, B., Wedlund, C. S., & Liliensten, J. 2021, *The ATMOCIAID database*
- 1041
- 1042
- 1043
- 1044 Gronoff, G., Liliensten, J., Desorgher, L., & Flückiger, E. 2009a, *Astronomy and Astrophysics*, Volume 506, Issue 2, 2009, pp.955-964, 506, 955
- 1045
- 1046
- 1047 Gronoff, G., Liliensten, J., & Modolo, R. 2009b, *Astronomy and Astrophysics*, Volume 506, Issue 2, 2009, pp.965-970, 506, 965
- 1048
- 1049
- 1050 Gronoff, G., Liliensten, J., Simon, C., et al. 2008, *A&A*, 482, 1015, number: 3 Publisher: EDP Sciences
- 1051
- 1052
- 1053 Gronoff, G., Liliensten, J., Simon, C., et al. 2007, *A&A*, 465, 641, number: 2 Publisher: EDP Sciences
- 1054
- 1055
- 1056 Gronoff, G., Rahmati, A., Simon Wedlund, C., et al. 2014, *Geophys. Res. Lett.*, 41, 4844
- 1057
- 1058
- 1059 Gronoff, G., Simon Wedlund, C., Mertens, C. J., et al. 2012a, *Journal of Geophysical Research (Space Physics)*, 117, A05309
- 1060
- 1061
- 1062 Gronoff, G., Simon Wedlund, C., Mertens, C. J., & Lillis, R. J. 2012b, *Journal of Geophysical Research (Space Physics)*, 117, A04306
- Gustin, J., Grodent, D., Gérard, J. C., & Clarke, J. T. 2002, *Icarus*, 157, 91
- Gustin, J., Grodent, D., Ray, L. C., et al. 2016, *Icarus*, 268, 215
- Gustin, J., Gérard, J. C., Grodent, D., et al. 2013, *Journal of Molecular Spectroscopy*, 291, 108
- Gérard, J.-C., Bonfond, B., Grodent, D., et al. 2014, *Journal of Geophysical Research: Space Physics*, 119, 9072, number: 11 [_eprint: https://onlinelibrary.wiley.com/doi/pdf/10.1002/2014JA020514](https://onlinelibrary.wiley.com/doi/pdf/10.1002/2014JA020514)
- Gérard, J.-C., Dols, V., Paresce, F., & Prangé, R. 1993, *Journal of Geophysical Research: Planets*, 98, 18793, [_eprint: https://onlinelibrary.wiley.com/doi/pdf/10.1029/93JE01334](https://onlinelibrary.wiley.com/doi/pdf/10.1029/93JE01334)
- Gérard, J. C., Grodent, D., Dols, V., et al. 1994, *Science*, 266, 1675, publisher: American Association for the Advancement of Science
- Gérard, J.-C. & Singh, V. 1982, *Journal of Geophysical Research: Space Physics*, 87, 4525, [_eprint: https://onlinelibrary.wiley.com/doi/pdf/10.1029/JA087iA06p04525](https://onlinelibrary.wiley.com/doi/pdf/10.1029/JA087iA06p04525)
- Hansen, C. J., Bolton, S. J., Matson, D. L., Spilker, L. J., & Lebreton, J.-P. 2004, *Icarus*, 172, 1
- Harris, W., Clarke, J. T., McGrath, M. A., & Ballester, G. E. 1996, *Icarus*, 123, 350
- Hess, S. L. G., Bonfond, B., Chantry, V., et al. 2013, *Planetary and Space Science*, 88, 76
- Hess, S. L. G., Delamere, P., Dols, V., Bonfond, B., & Swift, D. 2010, *Journal of Geophysical Research: Space Physics*, 115, [_eprint: https://onlinelibrary.wiley.com/doi/pdf/10.1029/2009JA014928](https://onlinelibrary.wiley.com/doi/pdf/10.1029/2009JA014928)
- Hinson, D. P., Twicken, J. D., & Karayel, E. T. 1998, *Journal of Geophysical Research: Space Physics*, 103, 9505, [_eprint: https://onlinelibrary.wiley.com/doi/pdf/10.1029/97JA03689](https://onlinelibrary.wiley.com/doi/pdf/10.1029/97JA03689)
- Hue, V., Giles, R. S., Gladstone, G. R., et al. 2021, *Journal of Astronomical Telescopes, Instruments, and Systems*, 7, 044003
- Hue, V., Gladstone, G. R., Greathouse, T. K., et al. 2019, *AJ*, 157, 90
- Hue, V., Hersant, F., Cavalié, T., Dobrijevic, M., & Sinclair, J. A. 2018, *Icarus*, 307, 106
- Jonin, C., Liu, X., Ajello, J. M., James, G. K., & Abgrall, H. 2000, *The Astrophysical Journal Supplement Series*, 129, 247, aDS Bibcode: 2000ApJS..129..247J
- Kameta, K., Kouchi, N., Ukai, M., & Hatano, Y. 2002, *Journal of Electron Spectroscopy and Related Phenomena*, 123, 225
- Kim, Y. H., Fox, J. L., & Porter, H. S. 1992, *Journal of Geophysical Research: Planets*, 97, 6093, [_eprint: https://onlinelibrary.wiley.com/doi/pdf/10.1029/92JE00454](https://onlinelibrary.wiley.com/doi/pdf/10.1029/92JE00454)
- Kingston, A. E. & Walters, H. R. J. 1980, *Journal of Physics B: Atomic and Molecular Physics*, 13, 4633
- Krupp, N. 2007, *Science*, 318, 216, publisher: American Association for the Advancement of Science
- Lathuillere, C., Blelly, P. L., Liliensten, J., & Gaimard, P. 1997, *Advances in Space Research*, 20, 1699
- Lee, A. Y. T., Yung, Y. L., Cheng, B.-M., et al. 2001, *The Astrophysical Journal*, 551, L93, publisher: IOP Publishing
- Liliensten, J., Kofman, W., Wisenberg, J., Oran, E. S., & DeVore, C. R. 1989, *Annales Geophysicae*, 7, 83, aDS Bibcode: 1989AnGeo...7...83L
- Liliensten, J., Simon, C., Witasse, O., et al. 2005a, *Icarus*, 174, 285
- Liliensten, J., Witasse, O., Simon, C., et al. 2005b, *Geophysical Research Letters*, 32, [_eprint: https://onlinelibrary.wiley.com/doi/pdf/10.1029/2004GL021432](https://onlinelibrary.wiley.com/doi/pdf/10.1029/2004GL021432)
- Liu, X., Ahmed, S. M., Multari, R. A., James, G. K., & Ajello, J. M. 1995, *The Astrophysical Journal Supplement Series*, 101, 375, aDS Bibcode: 1995ApJS..101..375L
- Liu, X., Shemansky, D. E., Abgrall, H., et al. 2003, *Journal of Physics B: Atomic, Molecular and Optical Physics*, 36, 173
- Liu, X., Shemansky, D. E., Abgrall, H., et al. 2002, *The Astrophysical Journal Supplement Series*, 138, 229
- Liu, X., Shemansky, D. E., Ahmed, S. M., James, G. K., & Ajello, J. M. 1998, *Journal of Geophysical Research: Space Physics*, 103, 26739, [_eprint: https://onlinelibrary.wiley.com/doi/pdf/10.1029/98JA02721](https://onlinelibrary.wiley.com/doi/pdf/10.1029/98JA02721)
- Livengood, T. A., Moos, H. W., Ballester, G. E., & Prangé, R. M. 1992, *Icarus*, 97, 26
- Mauk, B. H., Clark, G., Gladstone, G. R., et al. 2020, *Journal of Geophysical Research: Space Physics*, 125, e2019JA027699, [_eprint: https://onlinelibrary.wiley.com/doi/pdf/10.1029/2019JA027699](https://onlinelibrary.wiley.com/doi/pdf/10.1029/2019JA027699)
- Mauk, B. H., Haggerty, D. K., Paranicas, C., et al. 2017, *Nature*, 549, 66, number: 7670 Publisher: Nature Publishing Group
- Mauk, B. H., Haggerty, D. K., Paranicas, C., et al. 2018, *Geophysical Research Letters*, 45, 1277, aDS Bibcode: 2018GeoRL..45.1277M
- Menager, H. 2011, PhD thesis, thèse de doctorat dirigée par Liliensten, Jean Astrophysique et milieux dilués Grenoble 2011
- Menager, H., Barthélemy, M., & Liliensten, J. 2010, *Astronomy and Astrophysics*, 509, A56
- Moses, J. I., Fouchet, T., Bézard, B., et al. 2005, *Journal of Geophysical Research: Planets*, 110, number: E8 [_eprint: https://agupubs.onlinelibrary.wiley.com/doi/pdf/10.1029/2005JE002411](https://agupubs.onlinelibrary.wiley.com/doi/pdf/10.1029/2005JE002411)
- Muse, J., Silva, H., Lopes, M. C. A., & Khakoo, M. A. 2008, *Journal of Physics B: Atomic, Molecular and Optical Physics*, 41, 095203
- Nakayama, T. & Watanabe, K. 2004, *The Journal of Chemical Physics*, 120, 558
- Nicholson, W. P., Gronoff, G., Liliensten, J., Aylward, A. D., & Simon, C. 2009, *Monthly Notices of the Royal Astronomical Society*, 400, 369
- Perry, J. J., Kim, Y. H., Fox, J. L., & Porter, H. S. 1999, *Journal of Geophysical Research: Planets*, 104, 16541, [_eprint: https://onlinelibrary.wiley.com/doi/pdf/10.1029/1999JE900022](https://onlinelibrary.wiley.com/doi/pdf/10.1029/1999JE900022)
- Porter, H. S., Varosi, F., & Mayr, H. G. 1987, *Journal of Geophysical Research: Space Physics*, 92, 5933, [_eprint: https://onlinelibrary.wiley.com/doi/pdf/10.1029/JA092iA06p05933](https://onlinelibrary.wiley.com/doi/pdf/10.1029/JA092iA06p05933)
- Prangé, R., Rego, D., Pallier, L., et al. 1998, *Journal of Geophysical Research: Planets*, 103, 20195, [_eprint: https://onlinelibrary.wiley.com/doi/pdf/10.1029/98JE01128](https://onlinelibrary.wiley.com/doi/pdf/10.1029/98JE01128)

- 1141 Rees, M. H. 1989, *Physics and Chemistry of the Upper Atmosphere* (Cambridge
1142 University Press), google-Books-ID: qNDSsYwdrCs
- 1143 Rego, D., Clarke, J. T., Jaffel, L. B., et al. 2001, *Icarus*, 150, 234
- 1144 Russell, C. T. 1993, *Reports on Progress in Physics*, 56, 687
- 1145 Salveter, A., Saur, J., Clark, G., & Mauk, B. H. 2022, *Journal of*
1146 *Geophysical Research: Space Physics*, 127, e2021JA030224, _eprint:
1147 <https://onlinelibrary.wiley.com/doi/pdf/10.1029/2021JA030224>
- 1148 Saur, J., Janser, S., Schreiner, A., et al. 2018, *Journal of*
1149 *Geophysical Research: Space Physics*, 123, 9560, _eprint:
1150 <https://onlinelibrary.wiley.com/doi/pdf/10.1029/2018JA025948>
- 1151 Scherer, K., Fichtner, H., & Lazar, M. 2018, *Europhysics Letters*, 120, 50002,
1152 publisher: EDP Sciences, IOP Publishing and Società Italiana di Fisica
- 1153 Schunk, R. W. & Hays, P. B. 1971, *Planetary and Space Science*, 19, 113
- 1154 Schunk, R. W., Hays, P. B., & Yukikazu, I. 1971, *Planetary and Space Science*,
1155 19, 125
- 1156 Simon, C., Liliensten, J., Moen, J., et al. 2007, *Annales Geophysicae*, 25, 661
- 1157 Simon, C., Witasse, O., Leblanc, F., Gronoff, G., & Bertaux, J. L. 2009, *Planetary*
1158 *and Space Science*, 57, 1008
- 1159 Sinclair, J. A., Orton, G. S., Greathouse, T. K., et al. 2018, *Icarus*, 300, 305, aDS
1160 Bibcode: 2018Icar..300..305S
- 1161 Singhal, R. P., Chakravarty, S. C., Bhardwaj, A., & Prasad, B. 1992,
1162 *Journal of Geophysical Research: Planets*, 97, 18245, _eprint:
1163 <https://onlinelibrary.wiley.com/doi/pdf/10.1029/92JE01894>
- 1164 Stamnes, K. & Rees, M. H. 1983a, *Geophysical Research Letters*, 10, 309,
1165 _eprint: <https://onlinelibrary.wiley.com/doi/pdf/10.1029/GL010i004p00309>
- 1166 Stamnes, K. & Rees, M. H. 1983b, *Journal of Geo-*
1167 *physical Research: Space Physics*, 88, 6301, _eprint:
1168 <https://onlinelibrary.wiley.com/doi/pdf/10.1029/JA088iA08p06301>
- 1169 Stamnes, K., Tsay, S.-C., Wiscombe, W., & Jayaweera, K. 1988, *Applied Optics*,
1170 27, 2502, number: 12 Publisher: Optica Publishing Group
- 1171 Swartz, W. E., Nisbet, J. S., & Green, A. E. S. 1971, *Jour-*
1172 *nal of Geophysical Research* (1896-1977), 76, 8425, _eprint:
1173 <https://onlinelibrary.wiley.com/doi/pdf/10.1029/JA076i034p08425>
- 1174 Trafton, L. M., Dols, V., Gérard, J.-C., et al. 1998, *The Astrophysical Journal*,
1175 507, 955, publisher: IOP Publishing
- 1176 Trafton, L. M., Gerard, J. C., Munhoven, G., & Waite, Jr., J. H. 1994, *The Astro-*
1177 *physical Journal*, 421, 816, aDS Bibcode: 1994ApJ...421..816T
- 1178 Waite, J. H., Cravens, T. E., Kozyra, J., et al. 1983, *Journal*
1179 *of Geophysical Research: Space Physics*, 88, 6143, _eprint:
1180 <https://onlinelibrary.wiley.com/doi/pdf/10.1029/JA088iA08p06143>
- 1181 Wedde, T. & Strand, T. G. 1974, *Journal of Physics B: Atomic and Molecular*
1182 *Physics*, 7, 1091
- 1183 Wedlund, C. S., Gronoff, G., Liliensten, J., Ménager, H., & Barthélemy, M. 2011,
1184 *Annales Geophysicae*, 29, 187
- 1185 Witasse, O., Dutuit, O., Liliensten, J., et al. 2002,
1186 *Geophysical Research Letters*, 29, 104, _eprint:
1187 <https://onlinelibrary.wiley.com/doi/pdf/10.1029/2002GL014781>
- 1188 Witasse, O., Dutuit, O., Liliensten, J., et al. 2003, *Geophysical Research Letters*,
1189 30, _eprint: <https://onlinelibrary.wiley.com/doi/pdf/10.1029/2003GL017007>
- 1190 Wu, C. Y. R., Chen, F. Z., & Judge, D. L. 2001, *Jour-*
1191 *nal of Geophysical Research: Planets*, 106, 7629, _eprint:
1192 <https://onlinelibrary.wiley.com/doi/pdf/10.1029/2000JE001292>
- 1193 Yung, Y. L., Gladstone, G. R., Chang, K. M., Ajello, J. M., & Srivas-
1194 tava, S. K. 1982, *The Astrophysical Journal*, 254, L65, aDS Bibcode:
1195 1982ApJ...254L..65Y
- 1196 Zarka, P. 1998, *Journal of Geophysical Research: Planets*, 103, 20159, _eprint:
1197 <https://onlinelibrary.wiley.com/doi/pdf/10.1029/98JE01323>

Appendix A: Description of the electron transport model (TransPlanet)

In the context of the modeling work we performed for this study, we focused on the kinetic part of the code. This part calculates the ionization rates, atmospheric particle excited states, and emission rates caused by solar ultraviolet flux and the precipitation of magnetospheric electrons. The energy deposited by electrons when they interact with atmospheric particles is often modeled using two different approaches: the continuous loss approximation (Yung et al. 1982; Gérard & Singh 1982; Waite et al. 1983; Singhal et al. 1992) and the discrete loss approximation (Kim et al. 1992; Perry et al. 1999). Contrary to other models that use these types of approximation, the Trans* code describes the interaction between suprathermal electrons and neutral atmospheric particles by self-consistently solving the dissipative Boltzmann equation. Likewise, the originality of the Trans* solvers is that they are based on a radiative transfer solver, called DISORT (Stamnes et al. 1988). This is in sharp contrast with Monte Carlo transport models, and results in an accrued computation speed.

Boltzmann's equation describes the interactions between particles in a gas. This equation models binary collisions between solid spheres interacting at short distance. It also takes into account the discrete aspect of the energy loss that occurs with each collision. The secondary electrons produced during ionization by collisions between precipitating primary electrons and atmospheric particles are also taken into account using this equation, and are included in the suprathermal flux. All these interactions are therefore governed by the elastic and inelastic scattering cross sections of the electrons, thanks to the Boltzmann equation, extensively described and detailed by Stamnes & Rees (1983b), Gronoff (2009), Menager (2011), and Benmahi (2022).

Electrons precipitating into the atmosphere are represented by the distribution function $f(\mathbf{r}, \mathbf{v}, t)$ in phase space, where \mathbf{r} , \mathbf{v} , and t represent spatial position, velocity, and time, respectively, and f is given in cm^{-6}s^2 . Thus, the evolution of the distribution f is given by the nonconservative Boltzmann equation

$$\frac{\partial f}{\partial t} + \mathbf{v} \cdot \frac{\partial f}{\partial \mathbf{r}} + \frac{\partial}{\partial \mathbf{v}} \left(\frac{f\mathbf{X}}{m_e} \right) = Q, \quad (\text{A.1})$$

where Q represents a source function describing the electrons produced at position \mathbf{r} , velocity \mathbf{v} , and time t ; m_e is the electron mass; and \mathbf{X} is an external force applied to electrons in state (\mathbf{r}, \mathbf{v}) . In this electron transport model, the \mathbf{X} function is described by

$$\mathbf{X} = -n_e L(E) \frac{\mathbf{v}}{v}, \quad (\text{A.2})$$

where the function $L(E)$ describes the interaction by friction of thermalized electrons with suprathermal electrons, n_e is the number density of thermalized electrons, E is the energy of a suprathermal electron, and $v = \|\mathbf{v}\|$ is its velocity. Thus, the non-conservative nature of the Boltzmann equation arises from the nonconservative force \mathbf{X} . Trans* codes use the continuous friction function $L(E)$ proposed by Swartz et al. (1971) and established by Schunk et al. (1971) and Schunk & Hays (1971) to describe Coulomb interactions and Cerenkov emission. This function was therefore recommended by Stamnes & Rees (1983a) for the Trans* models.

In order to solve this equation, it is useful to reduce it to an equation relating to the flux I (which is given in $\text{cm}^{-2}\text{s}^{-1}\text{eV}^{-1}\text{sr}^{-1}$) by replacing the suprathermal electron distribution function f by the variable change $I(\mathbf{r}, E, \mathbf{u}, t) = \frac{v^2}{m_e} f(\mathbf{r}, \mathbf{v}, t)$, where $E = \frac{1}{2}mv^2$ is the kinetic energy of the electrons and $\mathbf{u} = \frac{\mathbf{v}}{v}$ is their direction. Thus, the equation becomes

$$\frac{1}{v} \frac{\partial I}{\partial t} + \frac{\mathbf{v}}{v} \cdot \frac{\partial I}{\partial \mathbf{r}} - n_e \frac{\partial}{\partial E} (L(E)I) = \frac{v^2}{m_e} Q. \quad (\text{A.3})$$

In the case of a plane-parallel geometry and assuming a stationary state, equation A.3, which represents the flux I along a magnetic field line \mathbf{B} , becomes

$$\mu \frac{\partial I(\tau, \mu, E)}{\partial \tau(z, E)} = -I(\tau, \mu, E) + \frac{n_e(z)}{\sum_k n_k(z) \sigma_k^{\text{tot}}(E)} \frac{\partial}{\partial E} (L(E)I(\tau, \mu, E)) + D(z, \mu, E) + P(z, \mu, E), \quad (\text{A.4})$$

where μ is the cosine of the angle between the magnetic field line and the direction of electron propagation, $n_k(z)$ [cm^{-3}] is the concentration of the atmospheric species k at altitude z , $\sigma_k^{\text{tot}}(E)$ [cm^2] is the total collision cross section between an electron and the species k at energy E , $\sigma_k^{\text{tot}}(E)$ is also the sum of the elastic and inelastic collision cross sections, and τ is a dimensionless quantity representing the electron scattering depth (similar to the optical depth in radiative transfer) defined by $\tau(z) = \int_z^{z_{\text{max}}} \sum_k n_k(z) \sigma_k^{\text{tot}}(E) \frac{dz}{\mu}$. $P(z, \mu, E)$ [$\text{cm}^{-2}\text{s}^{-1}\text{eV}^{-1}\text{sr}^{-1}$] is a source term for the primary electron flux introduced into the atmosphere in the (μ, E) state at altitude z ; this term includes incident magnetospheric electrons as well as photoelectrons produced by ionization caused by solar UV using a Beer-Lambert law of radiation absorption in the atmosphere. $D(z, \mu, E)$ [$\text{cm}^{-2}\text{s}^{-1}\text{eV}^{-1}\text{sr}^{-1}$] is a scattering term representing secondary electrons resulting from inelastic electron collisions between a primary electron and an atmospheric particle, as well as primary electrons whose energy has been dissipated by their interactions with atmospheric particles.

Appendix B: Examples of UVS spectra fitting

From the PJ32 spectral cube, we selected two small auroral zones in the main emission region between 50°N and 60°N and in the outer emission region at around 70°N and 125°W . In these two regions, the median emission angles are respectively about 20° and 45° . In Figures B.1 and B.2, we plot in red the UV emission spectra averaged over each of the selected regions. The measured CR ratio is around 5.5 in the main emission region and 3.7 in the outer emission region.

Using an initial mono-energetic electron flux distribution, we modeled the emission spectrum to obtain the same CR as the observed spectrum for each selected region. For the main emission region, we used a mono-energetic distribution with an average energy of 90 keV to reproduce the emission spectrum in blue (Fig. B.1) with a CR of around 5.51, which represents the best fit. For the outer emission region, we obtained the best fit by modeling the UV emission spectrum using a mono-energetic distribution with an average energy of 75 keV and a CR of around 3.52.

However, depending on the spectral resolution of an observation, the emission spectrum can be fitted using any initial flux

1301 distribution in the electron transport model. On the other hand,
 1302 at very high spectral resolution (typically ~ 0.0125 nm), the en-
 1303 ergy signature of electrons on spectral lines below 110 nm is
 1304 visible, and the choice of initial electron flux distribution will
 1305 result in drastically different emission spectra. This implies that,
 1306 in this case, there are extra free parameters that we are unable
 1307 to control in order to constrain the type of initial electron flux
 1308 distribution in auroral zones. Thus, only in situ measurements of
 1309 electron energy spectra can provide an answer to this problem.

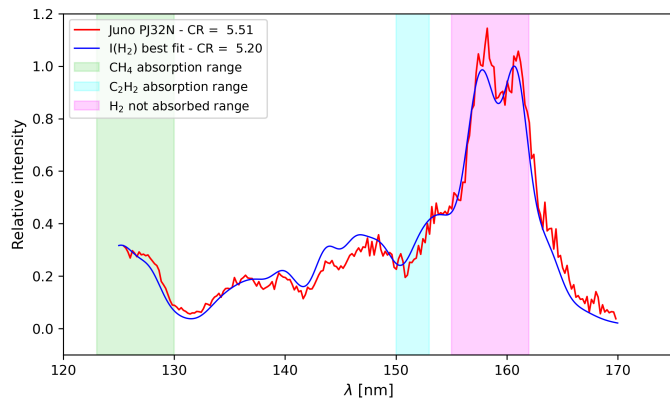


Fig. B.1. Examples of spectral fit (in blue) of a spectrum observed by Juno/UVS (in red) in a small region of the main emission in the southern arc of the northern auroral oval between 60°N and 50°N latitude. The median emission angle is around 20° , the observed CR is 5.50 and the spectral resolution is around 2.3 nm.

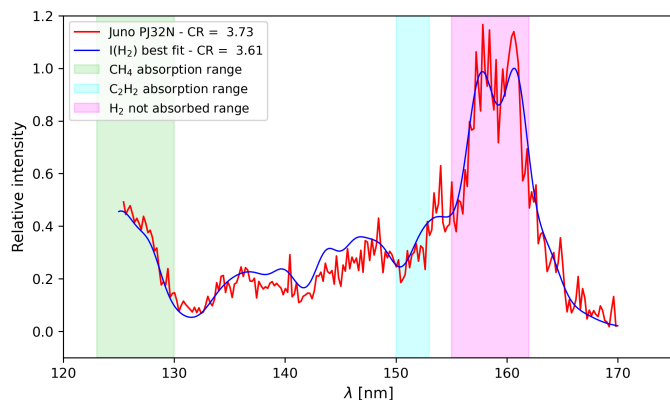


Fig. B.2. Examples of spectral fit of a spectrum observed by Juno/UVS in a small region of the outer emission in the northern auroral oval around position 70°N and 125°W SIII. The median emission angle is around 45° , the observed CR is 3.73 and the spectral resolution is estimated at around 2.3 nm.

1310 Appendix C: Regions of auroral emission and 1311 viewing angle maps

1312 In Fig. C.1 the magenta dots represent the pixels selected by our
 1313 S/N criterion, and thus represent UV emission from the auroral
 1314 region at the north pole. In the same way as above, we also used
 1315 this selection criterion to isolate the auroral emission from the
 1316 southern region.

1317 Figure C.2 displays maps of the emission angles observed by
 1318 UVS in the north and south polar regions. These emission angles
 1319 range from 0° to 50° in the south pole, and up to 80° in the north
 1320 pole.

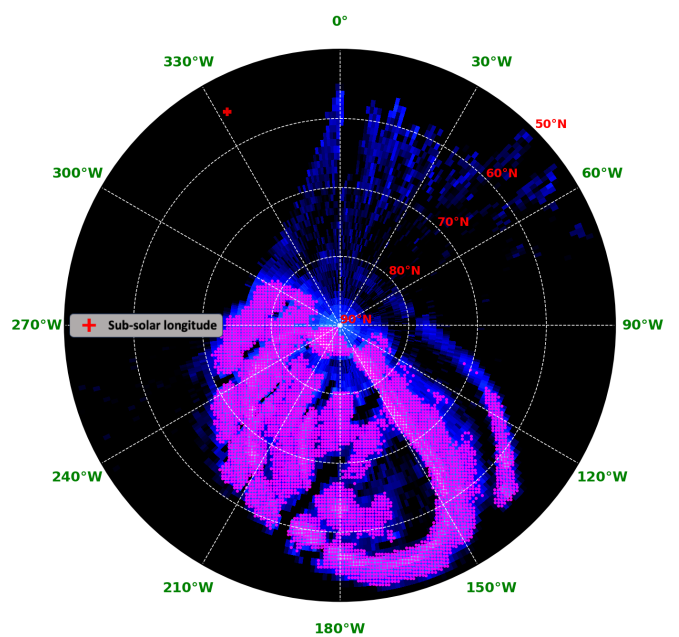


Fig. C.1. Isolated UV emission from Jupiter's auroral region, observed during PJ32 at the north pole by Juno/UVS. The magenta dots represent UV emission spectra where the unabsorbed part of the spectrum has a $S/N \geq 3$.

Appendix D: Modeling of CR relationship

1321

Appendix D.1: The dip magnetic angle and its impact on CR modeling

1322

1323

1324 The modeled CR as a function of the initial energy distribution of
 1325 the precipitating electrons is shown in Fig. D.1 for a fixed emis-
 1326 sion angle $\theta = 0^\circ$. These results assume a mono-energetic initial
 1327 electron flux distribution (Fig. D.1 left panel) and a kappa
 1328 distribution (Fig. D.1 right panel). In the case of a mono-energetic
 1329 distribution, the CR is modeled using 14 characteristic energy
 1330 points ranging from 1 keV to 220 keV. In the case of a kappa
 1331 distribution, we modeled the CR with only ten characteristic en-
 1332 ergy points ranging from 1 keV to 85 keV. We did this because
 1333 the CR increases more quickly than in the mono-energetic case
 1334 due to the broadening of the kappa distribution at high en-
 1335 ergies. The total precipitation flux for both distributions was set
 1336 to $Q_0 = 1 \text{ erg cm}^{-2}\text{s}^{-1}$ for all electron transport simulations.

1337 Electrons precipitating into the atmosphere are guided by
 1338 magnetic field lines. Depending on the magnetic dip angle ψ of
 1339 a given field line, these electrons will penetrate more deeply or
 1340 less deeply in the atmosphere. By varying ψ for a given char-
 1341 acteristic energy, the CR also varies. These variations in CR as a
 1342 function of angle ψ are less than 0.5 for $\psi \in [60^\circ, 75^\circ]$.

1343 In the present study we modeled $\text{CR}(E_0, \theta)$ as a function
 1344 of the median magnetic dip angle ψ in the auroral region for
 1345 each hemisphere. To this end, we used the JRM33 magnetic
 1346 field model of Jupiter (Connerney et al. 2022) to calculate the
 1347 magnetic dip angle at each point of the selected northern and
 1348 southern auroral regions (see the example in Fig. C.1). For each
 1349 electron energy distribution, the CR is modeled at the north and
 1350 south poles separately, and is represented by red and blue dots,
 1351 respectively (see Fig. D.1). For the north pole $\psi = 65.7^\circ$, and for
 1352 the south pole $\psi = 74.4^\circ$.

1353 For the case of mono-energetic electron flux distribution,
 1354 these results demonstrate the importance of taking into account
 1355 the geometry of the magnetic field lines at high energies because,

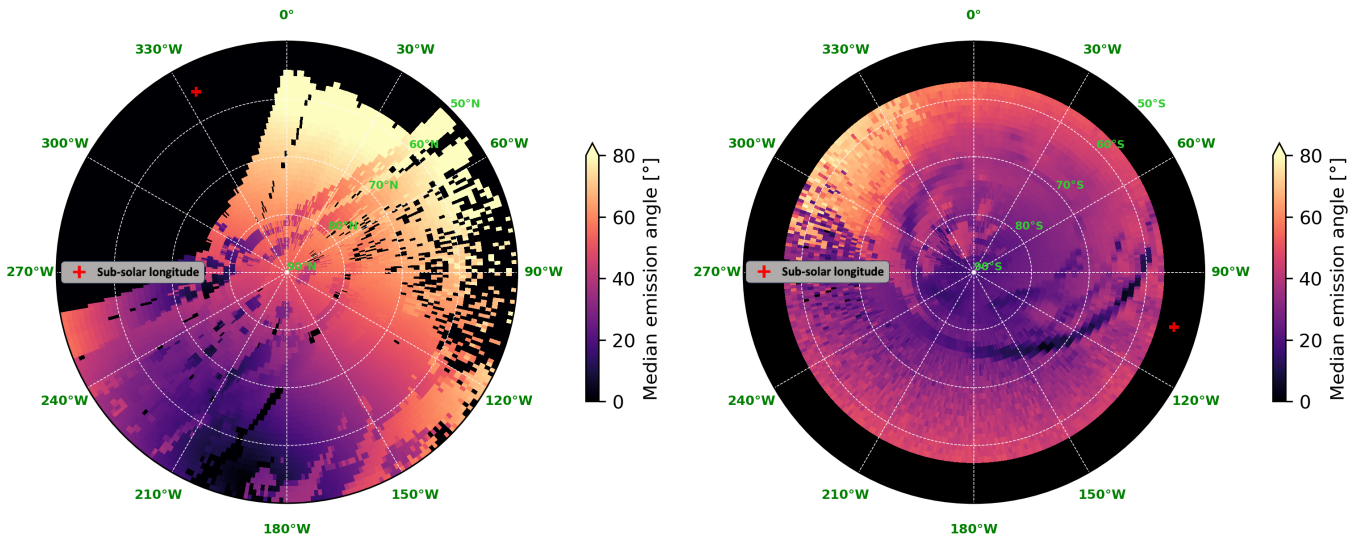


Fig. C.2. Maps of emission angles in the polar regions (left: northern hemisphere; right: southern hemisphere) observed during PJ32 when Juno was flying over the polar regions. Each point was observed with different emission angles along the probe’s trajectory. Thus, in these maps, each pixel represents the median value of the emission angles of the observed point.

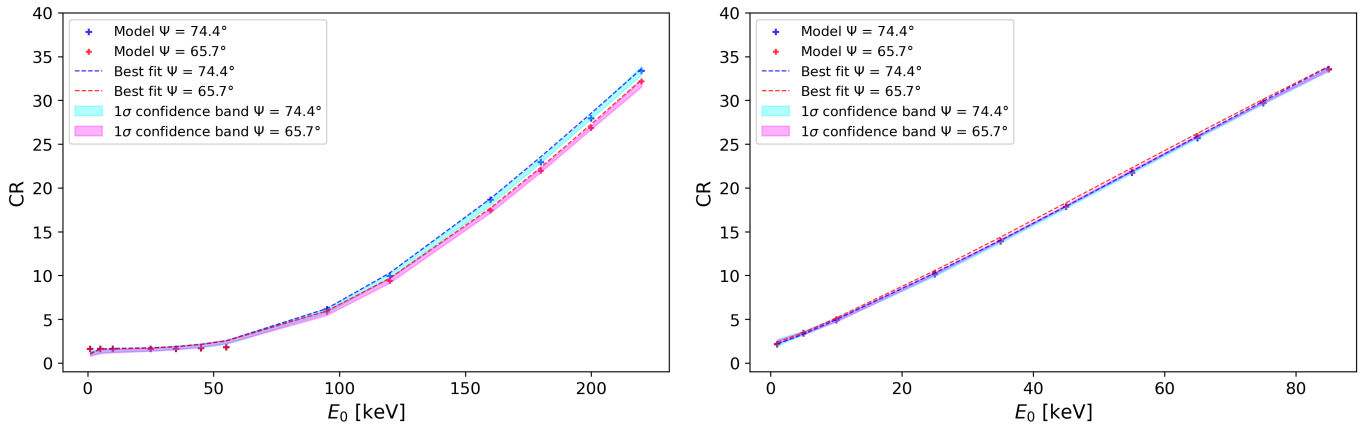


Fig. D.1. Example of modeled $CR(E_0)$ relationship. In the left panel the modeled relationship $CR(E_0)$ corresponds to the case of a mono-energetic initial electron flux distribution. Similarly, in the right panel the relationship $CR(E_0)$ corresponds to the case of a kappa initial distribution as a function of characteristic energy E_0 . The red and blue dots represent the modeled $CR(E_0)$ relationship, respectively, for the north pole with $\psi = 65.7^\circ$ and for the south pole with $\psi = 74.4^\circ$. The dotted red and blue lines represent the best fit for the north pole and south pole, respectively, using equation D.1.

1356 typically above 120 keV (see Fig. D.1), the relationship $CR(E_0)$
1357 becomes dependent on the magnetic dip angle. For the kappa
1358 distribution case, the evolution of the $CR(E_0)$ relationship is less
1359 influenced by the magnetic dip angle.

1360 Appendix D.2: Analytic formula and fit of the $CR(E_0, \theta)$ 1361 relationship

1362 Following the study of Gustin et al. (2016), we considered that
1363 $CR(E_0)$ follows a hyperbolic law at low energy and increases
1364 as a logarithmic law at high energy. Using our result from Fig.
1365 D.1, we derive a phenomenological relation $CR(E_0)$ in order to
1366 fit the CR modeling as a function of characteristic energy. This
1367 step allows us to obtain an analytical form of CR as a function of
1368 energy. In addition, thanks to a MCMC fit, it makes it possible
1369 to estimate the uncertainty on the modeled CR. Our analytical
1370 formulation of $CR(E_0)$ for a fixed θ emission angle is given by

$$CR(E_0) =$$

$$A \cdot C \cdot \left(\tanh\left(\frac{E_0 - E_c}{B} + 1\right) \right) \cdot \ln\left(\left(\frac{E_0}{D}\right)^\alpha + e\right)^\beta, \quad (\text{D.1})$$

where A is the minimum amplitude of the modeled CR; E_c is a
1371 threshold energy; and B , C , D , α , and β are fit parameters that
1372 constrain the shape of the curve throughout the energy range. 1373

To adjust these fitting parameters, we used the Python emcee
1374 package developed by Foreman-Mackey et al. (2013), which
1375 implements the MCMC method using the Metropolis-Hastings
1376 algorithm. The fitting configuration is characterized by 250
1377 Markov chains and 2500 iterations. These two parameters were
1378 determined after several runs of the burn-in size determination.
1379 We found that the Markov chains converge after 500–1000 iterations
1380 on average for all fit parameters for the mono-energetic
1381 and kappa distributions. The choice of 2500 iterations ensures
1382 convergence of the Markov chains in all cases. 1383

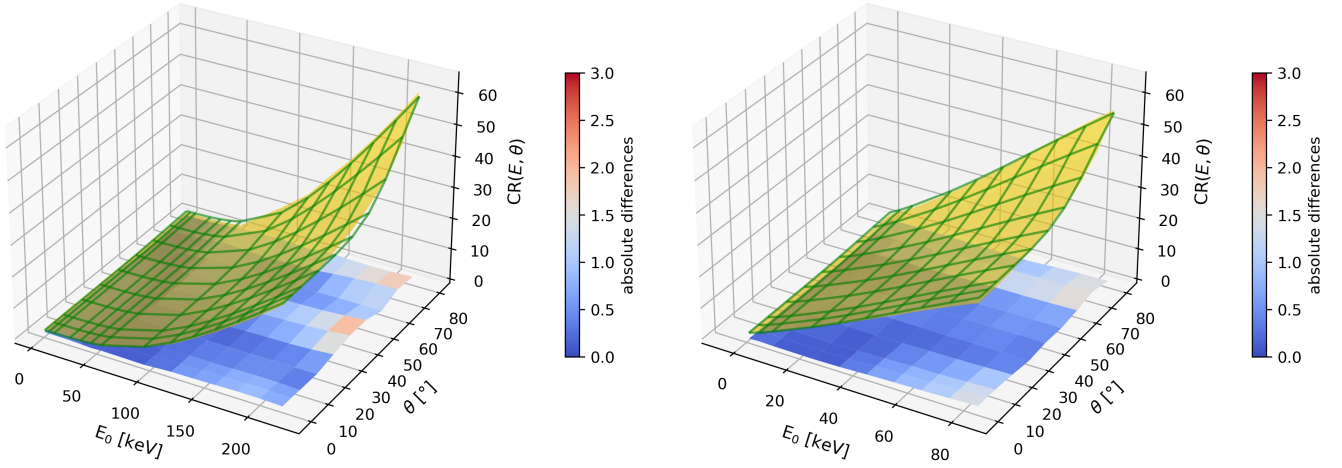


Fig. D.2. 3D representation of the $CR(E_0, \theta)$ modeled relationship for the case of a mono-energetic distribution (left panel) and for the case of a kappa distribution (right panel). Both relationships are calculated for the north pole (i.e., for $\psi = 65.7^\circ$). The green grid lines represent the fit of the modeled $CR(E_0, \theta)$ relationship. The colored surface (color bar from blue to red) represents the absolute difference between the modeled surface and the fit surface, with an average CR uncertainty of around 0.6 for the case of the mono-energetic distribution and an uncertainty of around 0.5 for the case of the kappa distribution.

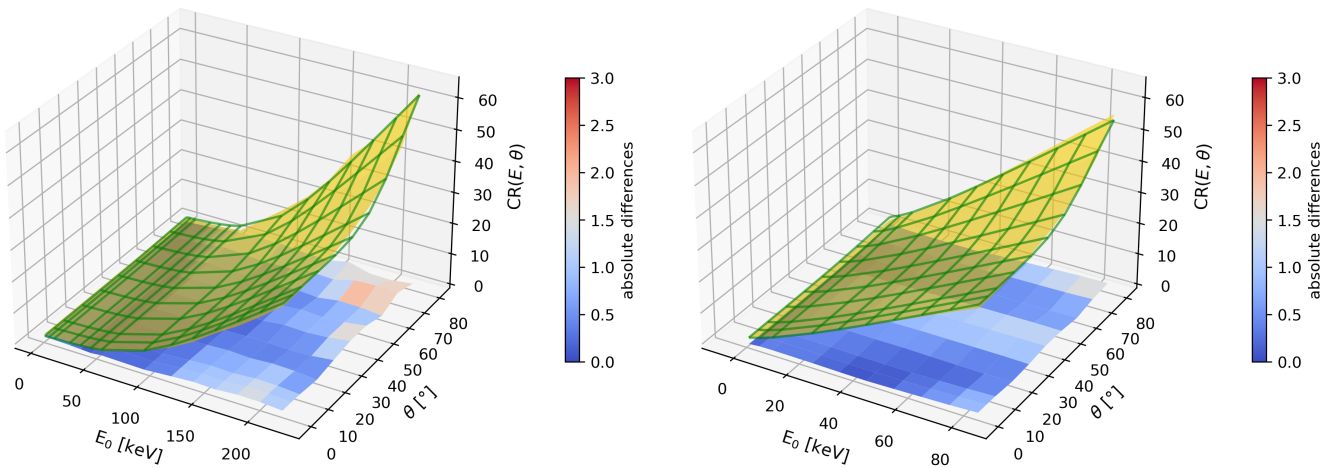


Fig. D.3. 3D representation of the $CR(E_0, \theta)$ modeled relationship for the case of mono-energetic distribution (left panel) and kappa distribution, south pole (i.e., for $\psi = 65.7^\circ$) and with the same conventions as Fig. D.2. The modeled CR uncertainty is estimated respectively at around 0.6 and 0.5 for both cases.

1384 In Fig. D.1, each CR-energy relationship that we modeled
 1385 (red dots for the north and blue dots for the south) was fitted
 1386 using the formula D.1. The magenta and cyan colored envelopes
 1387 represent the 1σ confidence band for each fit. This allowed us
 1388 to estimate the uncertainty of the CR modeling as a function of
 1389 energy. We found a mean CR uncertainty of around 0.5 for the
 1390 case of a mono-energetic distribution and 0.2 for the case of a
 1391 kappa distribution.

1392 For a variable emission angle θ and a fixed characteristic en-
 1393 ergy, we found that the $CR(\theta)$ relationship follows a sinusoidal
 1394 law. By taking into account the variability of the emission an-
 1395 gles and the characteristic energy simultaneously, the $CR(E_0, \theta)$

relationship is two-dimensional and is given by

1396

$$\begin{aligned}
 &CR(E_0, \theta) = \\
 &A \cdot C \cdot \left(\tanh\left(\frac{E_0 - E_c}{B}\right) + 1 \right) \cdot \ln\left(\left(\frac{E_0}{D}\right)^\alpha + e\right)^\beta, \\
 &\hspace{15em} (1 + \delta \cdot \sin(\theta)^\gamma) \quad (D.2)
 \end{aligned}$$

where δ and γ are additional fit parameters.

1397

As in the one-dimensional case (i.e., $CR(E_0)$), we modeled
 the $CR(E_0, \theta)$ relationship in a 2D (E_0, θ) grid. This grid is
 defined by 14 characteristic energy points ranging from 1 keV to
 220 keV for the case of a mono-energetic distribution, and 10
 characteristic energy points ranging from 1 keV to 85 keV for
 the case of a kappa distribution. For each characteristic energy
 E_0 , we also considered an emission angle grid θ of ten points
 ranging from 0° to 80° . This corresponds to modeling 140 UV

1405

1406 emission spectra, for each auroral region, to obtain a map of the
 1407 $CR(E_0, \theta)$ relationship for the case of mono-energetic distribu- 1468
 1408 tion. For the case of kappa distribution, this corresponds to mod- 1469
 1409 eling 100 UV emission spectra, for each auroral region, to obtain 1470
 1410 the maps of the $CR(E_0, \theta)$ relationship. 1471

1411 The electron transport modeling accuracy at each of the 1472
 1412 (E_0, θ) grid points (illustrated above) is evaluated by a total en- 1473
 1413 ergy conservation rate of the electrons precipitated in the model. 1474
 1414 Thus, for each electron transport simulation, the average rate of 1475
 1415 conservation of the total energy precipitated is about 99% for the 1476
 1416 case of a mono-energetic distribution and 99.5% for the case of a 1477
 1417 kappa distribution, which represents an energy loss, respectively, 1478
 1418 of 1% and 0.5%. All parameters were fitted in the same way 1479
 1419 as for the 1D case, using the same burn-in size for the MCMC 1480
 1420 method. 1481

1421 In Figures D.2 and D.3, we represent in yellow the results of 1482
 1422 the $CR(E_0, \theta)$ modeled relationship. To invert this phenomeno- 1483
 1423 logical relationship, we used the formula D.2 and fit its param- 1484
 1424 eters using the MCMC method explained in the text. In Table 1485
 1425 D.1, we presented the fit values of the parameters of the form- 1486
 1426 ula D.2 for each of the cases considered in our study. These 1487
 1427 parameters can be used directly in Eq. D.2 to map the character- 1488
 1428 istic energy of electrons precipitating in Jupiter’s auroral regions 1489
 1429 for any PJ. Δ_{CR} is the fitted noise of the modeled CR and cor- 1490
 1430 responds to the uncertainty of $CR(E_0, \theta)$. The average absolute 1491
 1431 difference between the fit and the model result is comparable to 1492
 1432 the uncertainty on the CR obtained by the MCMC method. 1493

1433 *Appendix D.3: Evolution of the $CR(E_0, \theta)$ relationship using* 1434 *different CH_4 abundance profiles*

1435 To evaluate the impact of methane distribution on the CR, we 1494
 1436 modeled the $CR(\langle E \rangle)$ relationship for an emission angle $\theta = 0^\circ$ 1495
 1437 and using two different CH_4 abundance profiles from the A 1496
 1438 and C eddy diffusion models of Moses et al. (2005) and Hue 1497
 1439 et al. (2018). These profiles are not representative of CH_4 auro- 1498
 1440 ral abundance, but have different homopauses compared to that 1499
 1441 of the Grodent et al. (2001) atmospheric model (see panel *a* in 1500
 1442 Fig. D.4). The $CR(\langle E \rangle)$ relationship was modeled for the cases of 1501
 1443 a kappa distribution and a mono-energetic distribution for elec- 1502
 1444 trons precipitating in auroral regions. 1503

1445 The results obtained are shown in panels *b* and *c* in Fig. D.4. 1504
 1446 This shows us that the CR depends on the CH_4 abundance profile 1505
 1447 used in our atmospheric model. Thus, depending on the CH_4 ho- 1506
 1448 mopause, the $CR(\langle E \rangle)$ relationship increases as a function of $\langle E \rangle$ 1507
 1449 more rapidly or less rapidly, as shown in Fig. D.4. The impact of 1508
 1450 this variability on the determination of the average energy map 1509
 1451 is also significant. 1510

1452 The results shown in panel *c* in Fig. D.4 show us the dif- 1511
 1453 ferences in the $CR(\langle E \rangle)$ relationships obtained for the case of a 1512
 1454 kappa distribution and the case of a mono-energetic distribution 1513
 1455 of precipitating electrons. Thus, using the Grodent et al. (2001) 1514
 1456 atmospheric model, we found that below 90 keV the $CR(\langle E \rangle)$ 1515
 1457 relationship obtained for the case of a mono-energetic distribu- 1516
 1458 tion overestimates the average energy of precipitating electrons. 1517
 1459 Above 90 keV, the same relationship underestimates the average 1518
 1460 energy of electrons precipitating in auroral regions. 1519

1461 By analyzing the ratio of the maps of the mean energies de- 1520
 1462 rived from two different electron distributions, a kappa distribu- 1521
 1463 tion and a mono-energetic one, we obtain the results presented 1522
 1464 in Fig. D.5. This result clarifies Fig. D.4 (panel *c*). It is notable 1523
 1465 that, in the main emission and polar emission zones, the mean 1524
 1466 energies derived from the kappa distribution are on average 3 to 1525
 1467 5 times higher than those derived from the mono-energetic dis- 1526

tribution for precipitating electrons in the northern and southern 1468
 auroral regions. In Fig. D.5, in the auroral regions where the ra- 1469
 tio of mean energies approaches ~ 1 , the mean energies derived 1470
 from the kappa distribution are around ~ 90 keV. In areas where 1471
 the ratio is less than 1, the mean energies associated with the 1472
 kappa distribution are strictly less than 90 keV. 1473

Table D.1. Fit parameters of Eq. D.2 for each of the cases considered in this study.

| Fit parameters | Kappa distribution (north pole) | Kappa distribution (south pole) | Mono-energetic distribution (north pole) | Mono-energetic distribution (south pole) |
|----------------|---------------------------------|---------------------------------|--|--|
| E_c [eV] | 2559 | 1417 | 2972 | 1511 |
| A | 1.59 | 1.69 | 1.88 | 1.8 |
| B [eV] | 10588 | 205693 | 800000 | 96641.40 |
| C | 1.48 | 1.15 | 0.59 | 0.51 |
| D [eV] | 17879 | 7642 | 56967 | 60847 |
| α | 1.69 | 1.2 | 3.16 | 3.15 |
| β | 1.93 | 2.28 | 2.15 | 2.07 |
| δ | 0.62 | 0.63 | 0.91 | 0.89 |
| γ | 6.63 | 6.74 | 7.9 | 7.9 |
| Δ_{CR} | 0.7 | 0.7 | 0.8 | 0.85 |

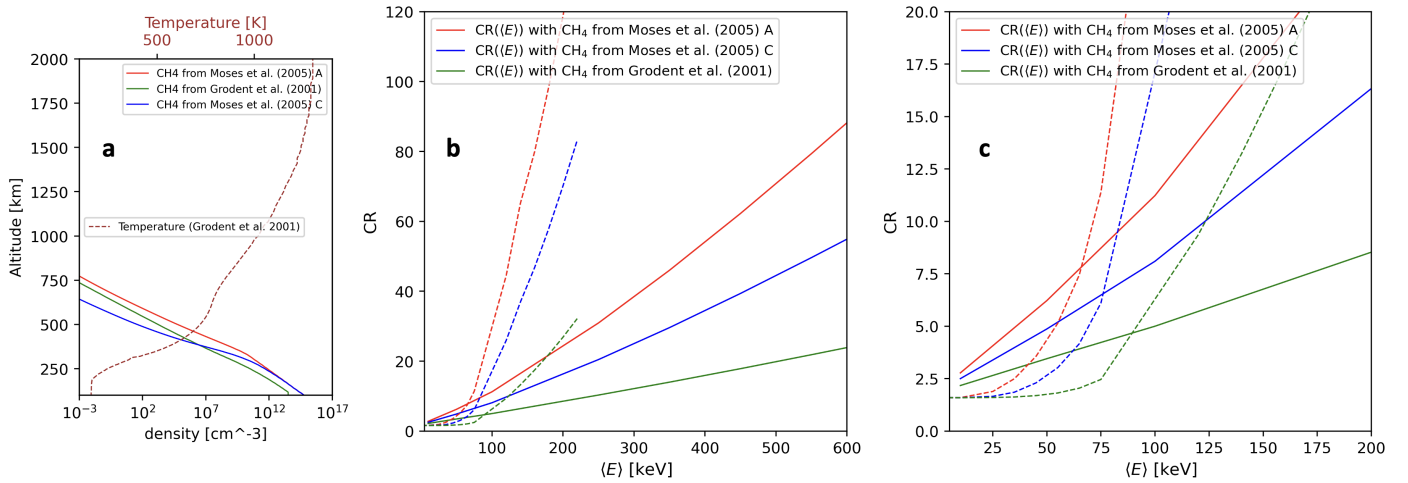


Fig. D.4. Model of the $CR(\langle E \rangle, \theta)$ relationship for $\theta = 0^\circ$ using different CH_4 abundance profiles. In panel **a**, the red, blue, and green solid lines represent the CH_4 abundance profile from, respectively, the A and C eddy diffusion models of Moses et al. (2005) and Hue et al. (2018), and the Grodent et al. (2001) atmospheric model. In panel **b** is represented the modeled $CR(\langle E \rangle)$ relationship. The solid lines represent the CR modeled using kappa electron flux distribution and the dotted lines by using a mono-energetic flux distribution. The color conventions are the same as described for panel **a**. In panel **c** a zoomed-in version of panel **b** is shown to distinguish between the various $CR(\langle E \rangle)$ results at low energy.

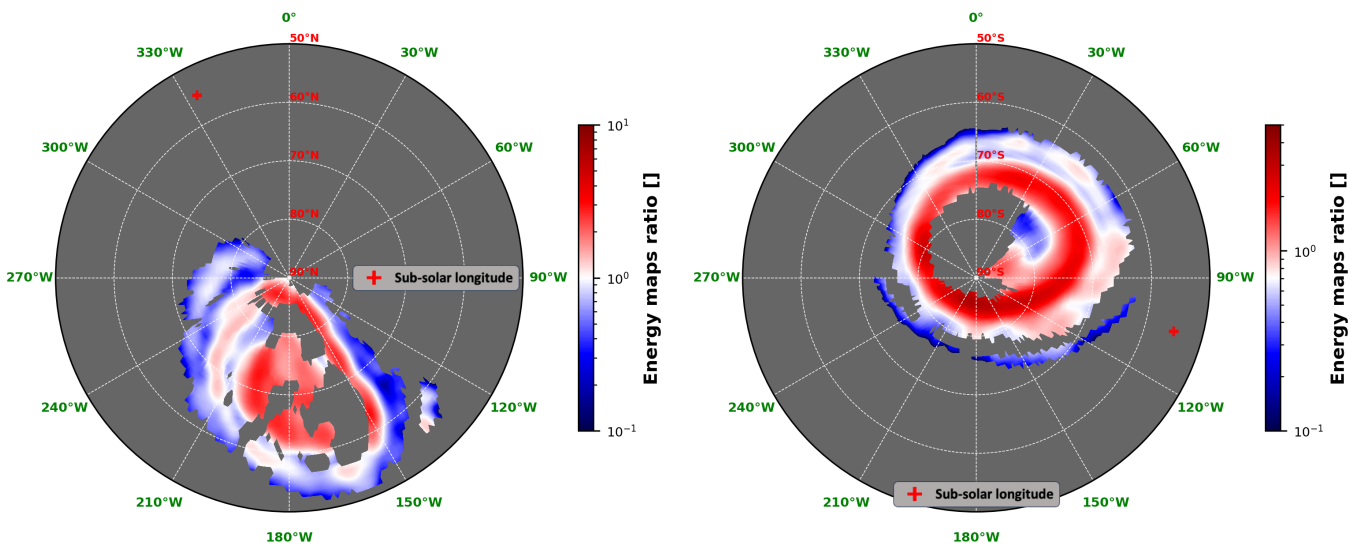


Fig. D.5. Ratio of average energy map for the kappa-distribution case (Fig. 9) to that of the monoenergetic case (Fig. 7). Left: Northern auroral region. Right: Southern auroral region.

